Transcriptional-translational conflict is a barrier to cellular transformation and cancer progression

Sujata Jana, Sandipan Brahma, Sonali Arora, Cynthia Wladyka, Patrick Hoang, Steven Blinka, Rowan Hough, Jessie Horn, Yuzhen Liu, Li-Jie Wang, et al.

Cancer Cell

Article

Transcriptional-translational conflict is a barrier to cellular transformation and cancer progression

Graphical abstract

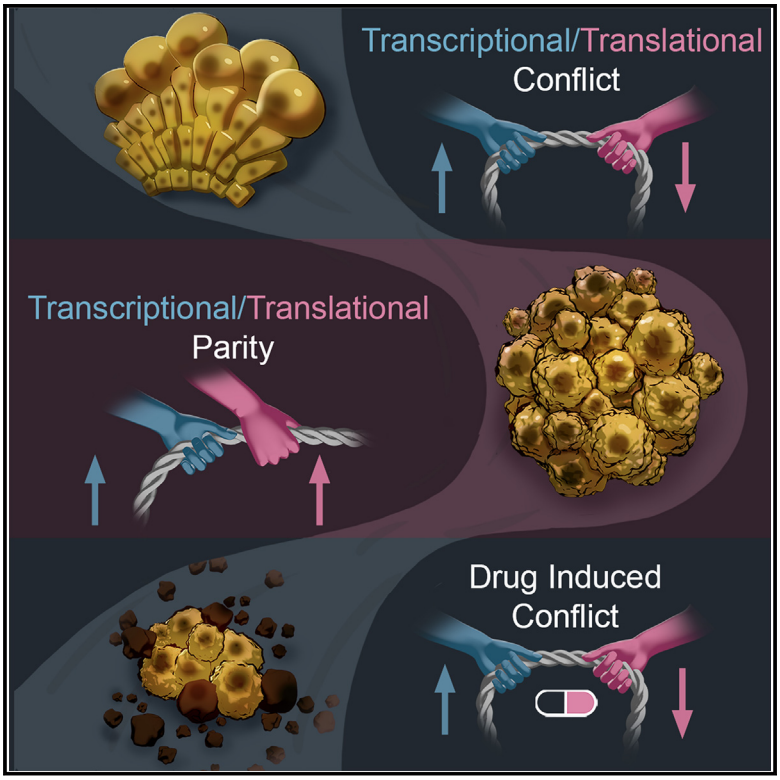

Highlights

- Transcriptional-translational conflict is tumor suppressive in bladder epithelium
- De-repression of translation elongation enables oncogenic phenotypes
- ARID1A-low tumors are sensitive to drug-induced transcriptional-translational conflict
- Impaired DNA damage response is a collateral effect of gene expression conflict

Authors

Sujata Jana, Sandipan Brahma, Sonali Arora, ..., Arvind R. Subramaniam, Steven Henikoff, Andrew C. Hsieh

Correspondence

ahsieh@fredhutch.org

In brief

Jana et al. reveal that ARID1A orchestrates a molecular conflict between gene-specific DNA transcription and mRNA translation in the bladder epithelium that is tumor suppressive. Transcriptional-translational conflict represents a new molecular stress that protects cells from transformation and must be overcome to enable cancer phenotypes.

Jana et al., 2023, Cancer Cell *41*, 853–870
May 8, 2023
https://doi.org/10.1016/j.ccell.2023.03.021

CellPress

Cancer Cell

CellPress
OPEN ACCESS

Article

Transcriptional-translational conflict is a barrier to cellular transformation and cancer progression

Sujata Jana,[1] Sandipan Brahma,[2] Sonali Arora,[1] Cynthia L. Wladyka,[1] Patrick Hoang,[1] Steven Blinka,[1,3] Rowan Hough,[1] Jessie L. Horn,[1] Yuzhen Liu,[1] Li-Jie Wang,[1] Philippe Depeille,[4] Eric Smith,[4] Robert B. Montgomery,[3] John K. Lee,[1,3,5] Michael C. Haffner,[1,5] Funda Vakar-Lopez,[5] Petros Grivas,[3] Jonathan L. Wright,[6] Hung-Ming Lam,[6] Peter C. Black,[7] Jeroen P. Roose,[4] Alexey G. Ryazanov,[8] Arvind R. Subramaniam,[2] Steven Henikoff,[2,9] and Andrew C. Hsieh[1,3,10,11,*]

[1]Human Biology Division, Fred Hutchinson Cancer Center, Seattle, WA 98109, USA
[2]Basic Science Division, Fred Hutchinson Cancer Center, Seattle, WA 98109, USA
[3]Department of Medicine, University of Washington, Seattle, WA 98195, USA
[4]Department of Anatomy, University of California, San Francisco, San Francisco, CA 94143, USA
[5]Department of Laboratory Medicine and Pathology, University of Washington, Seattle, WA 98195, USA
[6]Department of Urology, University of Washington, Seattle, WA 98915, USA
[7]Vancouver Prostate Centre, Department of Urologic Sciences, University of British Columbia, Vancouver, BC, Canada
[8]Department of Pharmacology, Rutgers Robert Wood Johnson Medical School, Piscataway, NJ 08854, USA
[9]Howard Hughes Medical Institute, Fred Hutchinson Cancer Center, Seattle, WA 98109, USA
[10]Genome Sciences, University of Washington, Seattle, WA 98915, USA
[11]Lead contact
*Correspondence: ahsieh@fredhutch.org
https://doi.org/10.1016/j.ccell.2023.03.021

SUMMARY

We uncover a tumor-suppressive process in urothelium called transcriptional-translational conflict caused by deregulation of the central chromatin remodeling component ARID1A. Loss of *Arid1a* triggers an increase in a nexus of pro-proliferation transcripts, but a simultaneous inhibition of the eukaryotic elongation factor 2 (eEF2), which results in tumor suppression. Resolution of this conflict through enhancing translation elongation speed enables the efficient and precise synthesis of a network of poised mRNAs resulting in uncontrolled proliferation, clonogenic growth, and bladder cancer progression. We observe a similar phenomenon in patients with ARID1A-low tumors, which also exhibit increased translation elongation activity through eEF2. These findings have important clinical implications because ARID1A-deficient, but not ARID1A-proficient, tumors are sensitive to pharmacologic inhibition of protein synthesis. These discoveries reveal an oncogenic stress created by transcriptional-translational conflict and provide a unified gene expression model that unveils the importance of the crosstalk between transcription and translation in promoting cancer.

INTRODUCTION

Major tumor suppressors such as *TP53*, *PTEN*, *APC*, and *PDCD4* are negative regulators of mRNA translation. Downregulation of each gene leads to an increase in mRNA-specific translation through cap-dependent and cap-independent mechanisms enabling cancer pathogenesis.[1–4] These findings suggest that a major function of tumor suppression is to downregulate the protein abundance of oncogenic gene networks. Recently, pan-cancer genome sequencing coupled with mechanistic work has uncovered a new class of tumor suppressors involved in chromatin remodeling.[5–8] In particular, components of ATP-dependent SWI/SNF family nucleosome remodeling complexes are mutated in 20% of human cancers.[9] Of these, the defining component of the BAF ATP-dependent SWI/SNF nucleosome remodeler called AT-rich interactive domain-containing protein 1A (ARID1A) is the most frequently mutated.[10] ARID1A is considered a tumor suppressor because genetic deletion leads to the transcriptional activation of oncogenic mRNAs, impairments in double-stranded DNA break repair and decatenation, and tumor progression.[5–7,11,12] It remains to be determined how ARID1A regulates protein synthesis in normal tissues.

We uncover a relationship between ARID1A and mRNA translation that challenges the prevailing dogma that tumor suppressors inhibit protein synthesis and introduces a tumor-suppressive process in urothelium called *transcriptional-translational conflict*. Although deletion of *Arid1a* promotes the transcription of a regulon of potentially oncogenic genes, this is countered by a paradoxical decrease in translation elongation rates. The resulting transcriptional-translational conflict specifically restrains the synthesis of pro-proliferation and mitogenic proteins and collateral DNA damage response (DDR) genes thereby

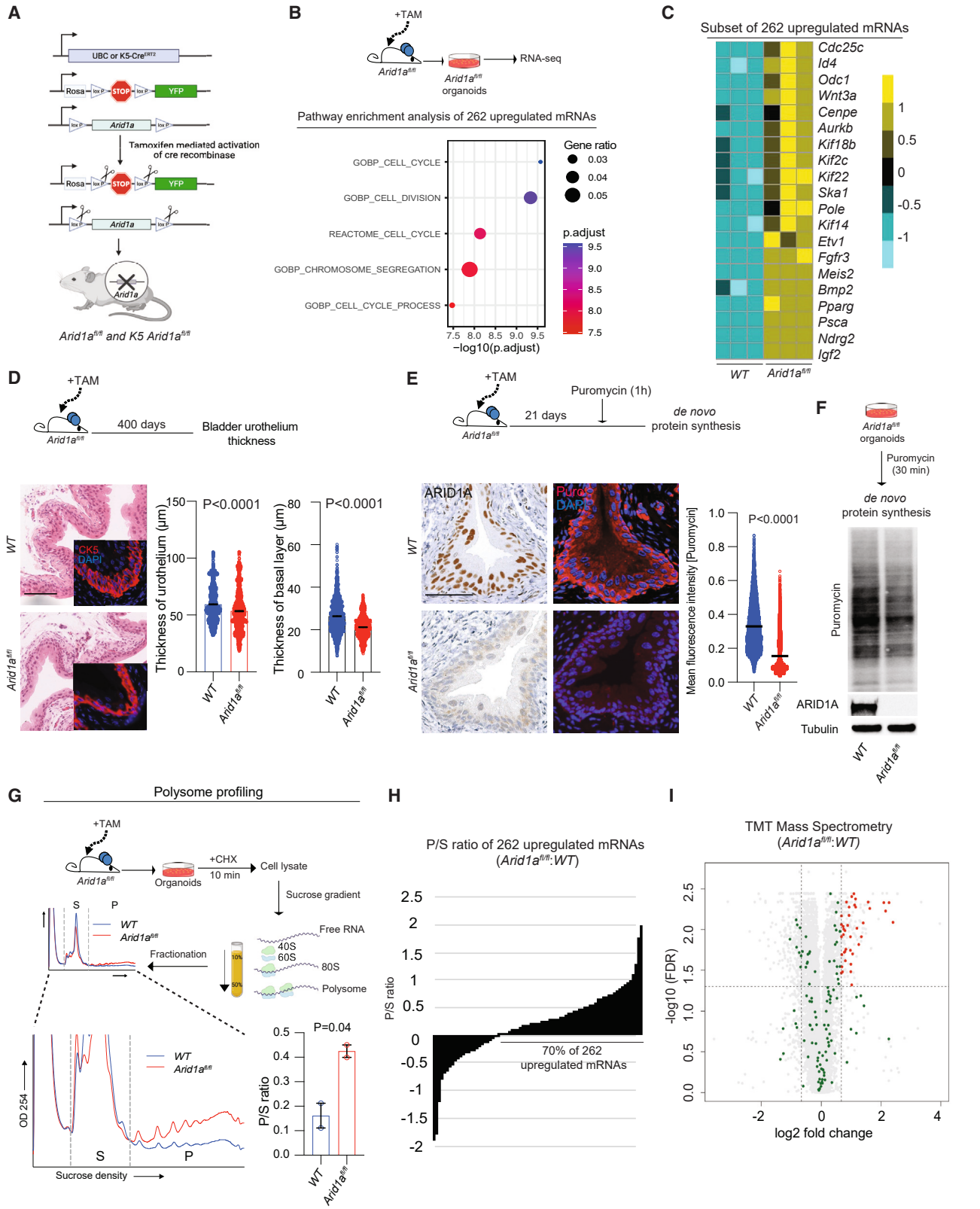

Figure 1. Loss of ARID1A leads to gene-specific transcriptional-translational conflict

Figure360▷ For a Figure360 author presentation of this figure, see https://doi.org/10.1016/j.ccell.2023.03.021.

(A) Schema of *UBC-Cre*^{ERT} and *K5-Cre*^{ERT} *Arid1a*$^{fl/fl}$ models.

(legend continued on next page)

preventing uncontrolled cell growth and cancer progression. Restoring translation elongation rates is needed to drive the tumor promoting properties of ARID1A loss. Remarkably, ARID1A-null tumors retain a memory of this translational dependence, which represents a selective therapeutic vulnerability. These findings reveal an oncogenic stress created by transcriptional-translational conflict that is a gatekeeper of urothelial homeostasis.

RESULTS

Loss of *Arid1a* leads to a gene-specific transcriptional-translational conflict in urothelium

To study the physiologic impact of deleting *Arid1a* on gene expression, we used a *UBC-Cre^{ERT2};ROSA-LSL-Yfp$^{KI/KI}$;Arid1a$^{LoxP/LoxP}$* mouse model (herein referred to as *Arid1a$^{fl/fl}$*) in which the administration of tamoxifen leads to deletion of ARID1A and expression of YFP in multiple tissues (Figure 1A). Within the urothelium, we observed a recombination efficiency of 83% (Figure S1A). We focused on the urothelium because bladder cancer is the 6th most common malignancy in humans,[13] and 25% of urothelial carcinoma patients exhibit *Arid1a* loss-of-function mutations.[14–16] Given that *Arid1a* loss has been shown to increase transcript levels of oncogenic genes in other tissues,[5] we sought to determine if the same is true within urothelial cells. We isolated basal cells, a cell of origin of invasive urothelial malignancies,[17,18] from wild-type (WT) and *Arid1a$^{fl/fl}$* bladders and conducted RNA sequencing (RNA-seq) (Figure S1B). We observed 262 upregulated mRNAs in *Arid1a$^{fl/fl}$* cells, and 80% of these were direct targets of *Arid1a* (Figure S1C; Table S1). Most overexpressed mRNAs were classified as regulators of cell proliferation (Figure 1B). Furthermore, these genes included aurora kinase B (*Aurkb*), insulin-like growth factor 2 (*Igf2*), fibroblast growth factor receptor 3 (*Fgfr3*), and ornithine decarboxylase 1 (*Odc1*), all of which are cancer drivers (Figure 1C).[19–22] Overexpression of *Aurkb*, *Igf2*, or *Fgfr3* in transgenic models is sufficient to drive uncontrolled cell growth and tumor formation.[23–25] Given these findings, we subsequently aged *Arid1a$^{fl/fl}$* mice for 400 days to determine if they develop bladder tumors. Despite the transcriptional activation of these gene networks, *Arid1a$^{fl/fl}$* mice exhibited a decrease in urothelial thickness characterized by fewer basal cells, and 0 of 9 mice developed tumors (Figure 1D).

These findings raise the important question of what might counter this gene expression program to prevent tumor initiation. One possibility is that *Arid1a* simultaneously controls protein synthesis. To measure protein synthesis rates *in vivo* we conducted a puromycin incorporation assay[26] and observed a 60% decrease in *de novo* protein synthesis in ARID1A-deficient urothelium (Figure 1E). We also generated an inducible *K5-Cre^{ERT2};ROSA-LSL-Yfp$^{KI/KI}$;Arid1a$^{LoxP/LoxP}$* model (referred to as *K5 Arid1a$^{fl/fl}$*) with 81%–87% recombination efficiency in basal cells in which we observed the same reduction in protein synthesis with striking cell type specificity (Figures S1D and S1E). To determine if this decrease was cell autonomous, we measured protein synthesis rates in organoids grown from *Arid1a$^{fl/fl}$* basal urothelium. Puromycin incorporation and ^{35}S-methionine incorporation were decreased in *Arid1a*-deficient organoids (Figures 1F and S1F). Although ARID1A loss increases a distinct network of pro-proliferative and potentially oncogenic network of mRNAs (Figure 1C), it is possible that it can also cause widespread transcriptional attenuation that would result in the perception of decreased protein synthesis.[27] We conducted RNA-seq of spike-in normalized[28] WT and *Arid1a$^{fl/fl}$* basal urothelial organoids. No widespread decrease in mRNA levels across the transcriptome were observed (Figure S1G). Last, we added back *Arid1a* in *Arid1a*-deficient organoids, which restored protein synthesis rates (Figure S1H). These findings demonstrate that *Arid1a* loss leads to opposing effects on transcription and translation, which is associated with an absence of tumor formation.

Next, we sought to determine how decreased *de novo* protein synthesis affects ribosome abundance on mRNA by polysome analysis.[29] We observed that *Arid1a$^{fl/fl}$* urothelial cells exhibited a significant increase in poly-ribosome abundance normalized to the sub-polysomal fraction (P/S ratio) (Figure 1G). Increased P/S ratio in the context of decreased protein synthesis can be caused by slower elongation rates.[3] To determine if ARID1A loss slows down translation elongation, we measured the ribosome half transit time.[30] We observed a half transit time of 85.5 ± 13 s in WT organoids and 143 ± 42 s in *Arid1a$^{fl/fl}$* organoids, which supports the idea that protein synthesis is disrupted at the level of elongation (Figure S1I).

These results raise the question of how decreased ribosome transit time affects the translation of distinct mRNA species, particularly the 262 mRNAs that are upregulated upon loss of *Arid1a* (Figure 1C). We sequenced ribosome bound mRNA to measure P/S ratios transcriptome-wide (Figure S1J). Strikingly, 70% of the 262 upregulated mRNAs in *Arid1a$^{fl/fl}$* cells exhibited increases in P/S ratio, providing genome-level evidence of a

(B) Pathway enrichment analysis of 262 mRNAs upregulated in the context of ARID1A loss.
(C) Heatmap showing a subset of pro-proliferation upregulated mRNAs from *Arid1a$^{fl/fl}$* organoids (>1.2 $\log_2$ fold change, FDR < 0.05).
(D) H&E staining (left with keratin 5, inset) and quantification (right) of mouse bladder urothelial thickness (total [n = 4/genotype] and basal cells [n = 3/genotype]) in 400-day-old WT and *Arid1a$^{fl/fl}$* mice. $p < 0.0001$ (t test).
(E) Immunohistochemistry (IHC) of ARID1A (left) and parallel sectioning and immunofluorescence (IF) of puromycin incorporation (right) in WT and *Arid1a$^{fl/fl}$* urothelium (DAPI, nuclei). n > 6/genotype, >8,900 cells/genotype. $p < 0.0001$ (t test).
(F) Puromycin immunoblot of WT and *Arid1a$^{fl/fl}$* urothelial organoids (replicate of 3).
(G) Schema of the polysome profiling assay (top). Polysome tracing showing an increase in polysome accumulation (left) and quantification showing an increase in the polysome (P) to sub-polysome (S) ratio (mean ± SEM). n = 2/genotype, t test.
(H) Waterfall plot showing polysome (P) to sub-polysome (S) ratio of 262 upregulated oncogenic mRNAs in *Arid1a$^{fl/fl}$* mice.
(I) Volcano plot of TMT mass spectrometry showing that 70% of upregulated mRNAs (105 of 150; only 150 of the 262 genes were detected by TMT mass spectrometry) identified by RNA-seq (Figure 1C; Table S1) do not increase in protein abundance (<0.67 $\log_2$ fold change and/or FDR > 0.05, green dots) in *Arid1a$^{fl/fl}$* mice. Vertical lines demarcate $\log_2$ fold change ± 0.67, and horizontal line demarcates FDR < 0.05 or >0.05.
All scale bars, 100 μm. Also see Figure S1.

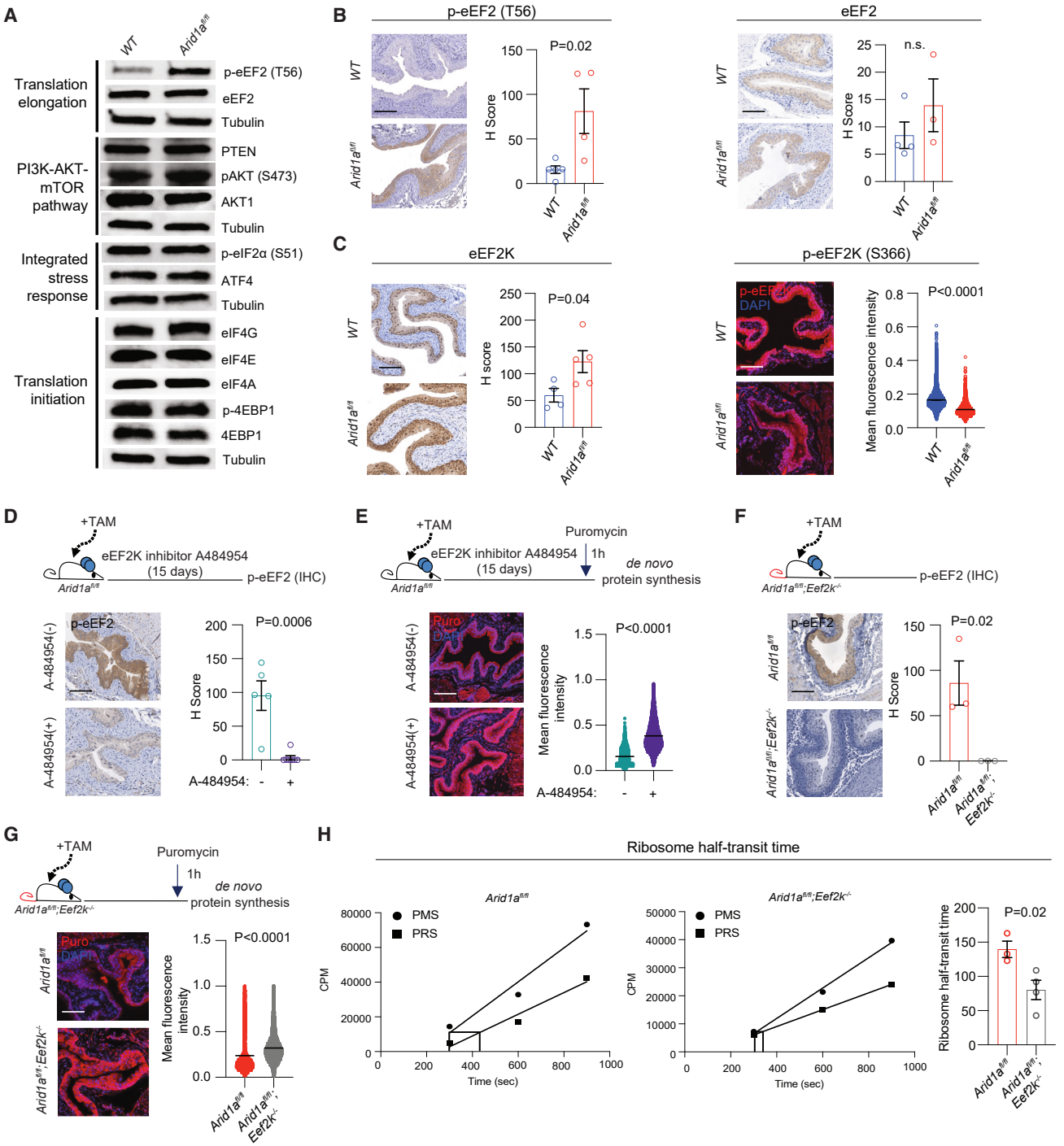

Figure 2. ARID1A is a positive regulator of mRNA translation elongation

(A) Immunoblots of regulators of mRNA translation in WT and *Arid1a*$^{fl/fl}$ urothelial organoids (replicate of 3).

(B) IHC and quantification of phospho-eEF2 (T56) and total eEF2 levels in WT and *Arid1a*$^{fl/fl}$ bladder urothelium. n ≥ 3/genotype. p = 0.02 (t test).

(C) IHC or IF and quantification of total eEF2K and phospho-eEF2K (S366) levels in WT and *Arid1a*$^{fl/fl}$ bladder urothelium. Violin plot represents >9,500 cells per genotype. n ≥ 4/genotype. p = 0.04 (left), p < 0.0001 (right) (t test).

(D and E) IHC analysis of phospho-eEF2 (T56) and IF analysis of puromycin incorporation after treatment with A-484954 in *Arid1a*$^{fl/fl}$ mice. Violin plot represents >7,700 cells/genotype. n ≥ 4/treatment arm p = 0.0006 (D), p < 0.0001 (E) (t test).

(F and G) IHC analysis of phospho-eEF2 (T56) and IF analysis of puromycin incorporation in *Arid1a*$^{fl/fl}$ and *Arid1a*$^{fl/fl}$;*Eef2k*$^{-/-}$ mice. Violin plot represents >6,000 cells/genotype. n ≥ 5/genotype. p = 0.02 (F), p < 0.0001 (G) (t test).

(legend continued on next page)

conflict between transcription of these genes and their translation (Figure 1H). Likewise, using tandem-mass-tag (TMT) mass spectrometry and immunoblot analysis, we found that 70% of the upregulated mRNAs also exhibited no increase in protein levels (Figures 1I and S1K; Table S2). These conflicted genes were enriched for guanine and cytosine nucleotides within their coding sequences (CDS), which is consistent with previous findings that higher guanine and cytosine content in the CDS is associated with slower codons (Figure S1L).[31] Thus, loss of ARID1A prevents the efficient translation of the majority of upregulated mRNAs, leading to transcriptional-translational conflict. These findings raise the important questions of how ARID1A regulates translation elongation.

ARID1A is a central regulator of eukaryotic elongation factor 2

Next, we sought to determine the mechanism by which ARID1A regulates translation elongation by conducting a candidate gene analysis of regulators of protein synthesis. We found no differences in 5.8S and 5S rRNA levels (Figure S2A). Next, we considered the PI3K signaling pathway (PTEN and AKT [total and phospho-S473]), the integrated stress response (phospho-eIF2α-S51 and ATF4), the eIF4F translation initiation complex (4EBP1 [total and phospho-T37/46], eIF4G, eIF4E, and eIF4A), and a translation elongation regulator (eEF2 [total and phospho-T56]).[32–34] Of these, only eEF2 phosphorylation was significantly increased upon *Arid1a* loss *in vitro* and *in vivo* (Figures 2A and 2B). eEF2 catalyzes GTP-dependent ribosome translocation during translation elongation, and its phosphorylation at T56 decreases protein synthesis rates.[35] The primary kinase responsible for eEF2 phosphorylation is the eukaryotic elongation factor 2 kinase (eEF2K), which regulates the cellular response to nutrient deprivation.[35–37] We measured eEF2K mRNA and protein levels and observed increases in both in *Arid1a*$^{fl/fl}$ urothelium, coinciding with a significant reduction in its inactive S366 phosphorylated form (Figures 2C, S2B, and S2C).

We used a pharmacogenetic strategy to determine if eEF2K activity regulates protein synthesis and elongation speed in *Arid1a*$^{fl/fl}$ urothelium. First, we treated *Arid1a*$^{fl/fl}$ mice with the eEF2K small-molecule inhibitor A-484954.[38] We observed an attenuation of eEF2 phosphorylation concomitant to restoration of protein synthesis in *Arid1a*$^{fl/fl}$ bladders (Figures 2D, 2E, and S2D). Next, we intercrossed *Arid1a*$^{fl/fl}$ and *Eef2k*$^{-/-}$ mice[39] to develop the *Arid1a*$^{fl/fl}$;*Eef2k*$^{-/-}$ mouse model in which eEF2 can no longer be phosphorylated (Figures 2F and S2E). We found that loss of *Eef2k* restores protein synthesis in *Arid1a*-deficient urothelium (Figure 2G). Furthermore, we determined that loss of *Eef2k* restores translation elongation rates in *Arid1a*$^{fl/fl}$;*Eef2k*$^{-/-}$ organoids back to WT levels in a cell-autonomous manner (ribosome half transit time of 80.2 ± 28 s) (Figures 2H and S1I). These data show that ARID1A maintains mRNA translation elongation by promoting eEF2 activity through downregulation of eEF2K. However, in the context of ARID1A loss, eEF2 activity decreases leading to slower ribosome transit time and a conflict between upregulated transcripts and their subsequent translation.

RASGRP1 is necessary to maintain eEF2 activity

Next, we sought to determine how ARID1A negatively regulates eEF2K activity. We have shown that ARID1A deficiency leads to a decrease in eEF2K phosphorylation at serine 366 (Figure 2C). The decrease of this inhibitory post-translational modification of eEF2K leads to an increase in eEF2 phosphorylation.[40] The MAP kinase (MAPK) and PI3K-AKT-mTOR signaling pathways converge on eEF2K S366 (Figure 3A).[40] In addition, an AMP kinase (AMPK) activating eEF2K phosphorylation site at serine 398 has also been described.[41] We found that ARID1A loss in urothelial organoids does not decrease PI3K-AKT-mTOR signaling or increase AMPK activity, suggesting these pathways are not responsible for the increase in eEF2 phosphorylation caused by ARID1A deficiency (Figures 2A and S3A). However, MEK1/2 (S217/221), ERK (T202/Y204), and p90RSK (S380) phosphorylation levels decreased in *Arid1a*-deficient urothelium without affecting total protein abundance or transcript levels (Figures 3B, S3B, and S3C). This finding suggests that the MAPK pathway is downregulated in *Arid1a*-deficient bladder urothelium which may affect eEF2K activity.

To determine how ARID1A controls the MAPK pathway, we measured mRNA abundance of MAPK regulators in WT and *Arid1a*$^{fl/fl}$ urothelial organoids. Surveying components in the Ras-MAPK pathway, we found no difference in expression of *Hras*, *Kras*, *Nras*, *Shc1*, *Src*, *Braf*, *Craf*, or *Sos1* (Figure 3C). However, *Rasgrp1* transcript levels were decreased by 80%, and RASGRP1 protein abundance was also decreased in *Arid1a*-deficient urothelium (Figures 3C, 3D, and S3D). Furthermore, ARID1A binds to the *Rasgrp1* promoter in WT urothelial cells (Figure 3E), and *Rasgrp1* mRNA and protein levels were restored by adding back ARID1A in *Arid1a*$^{fl/fl}$ organoids (Figures S3E and S3F). RASGRP1 is a diacylglycerol-regulated RasGEF, which activates the MAPK pathway with functions in T cells, T cell leukemia, and the intestinal epithelium.[42–45] However, its role in the urothelium is unknown. To determine if the decrease in RASGRP1 can increase eEF2K activity, we measured eEF2 phosphorylation in *Rasgrp1*$^{-/-}$ urothelium. Strikingly, *Rasgrp1*$^{-/-}$ urothelium exhibited a significant increase in eEF2 phosphorylation (Figures 3F and 3G), independent of total eEF2 protein levels (Figure S3G), which is consistent with *Arid1a*$^{fl/fl}$ mice.

We next sought to delineate how ARID1A regulates *Rasgrp1* expression. We conducted CUT&Tag chromatin profiling of histone H3 trimethylation of lysine 27 (H3K27me3) because downregulation of SWI/SNF activity is associated with H3K27me3 accumulation and repression of distinct genes.[46,47] We observed that 2,558 gene promoters exhibited greater than 2-fold increases in the H3K27me3 in *Arid1a*$^{fl/fl}$ organoids (Figure S3H). Moreover, on a gene-specific level, H3K27me3 at the *Rasgrp1* promoter was enriched 4.5-fold in *Arid1a*-deficient urothelial organoids and decreased in ARID1A add-back

(H) Ribosome half-transit time in *Arid1a*$^{fl/fl}$ and *Arid1a*$^{fl/fl}$;*Eef2k*$^{-/-}$ organoids (linear regression, left panels). Bar graph (right) represents the average ribosome half-transit time of 3 independent experiments. PMS, post-mitochondrial supernatants (complete + nascent proteins); PRS, post-ribosomal supernatant (complete proteins). p = 0.02 (t test).

n.s., not significant. Scale bar, 100 μm; mean ± SEM. Also see Figure S2.

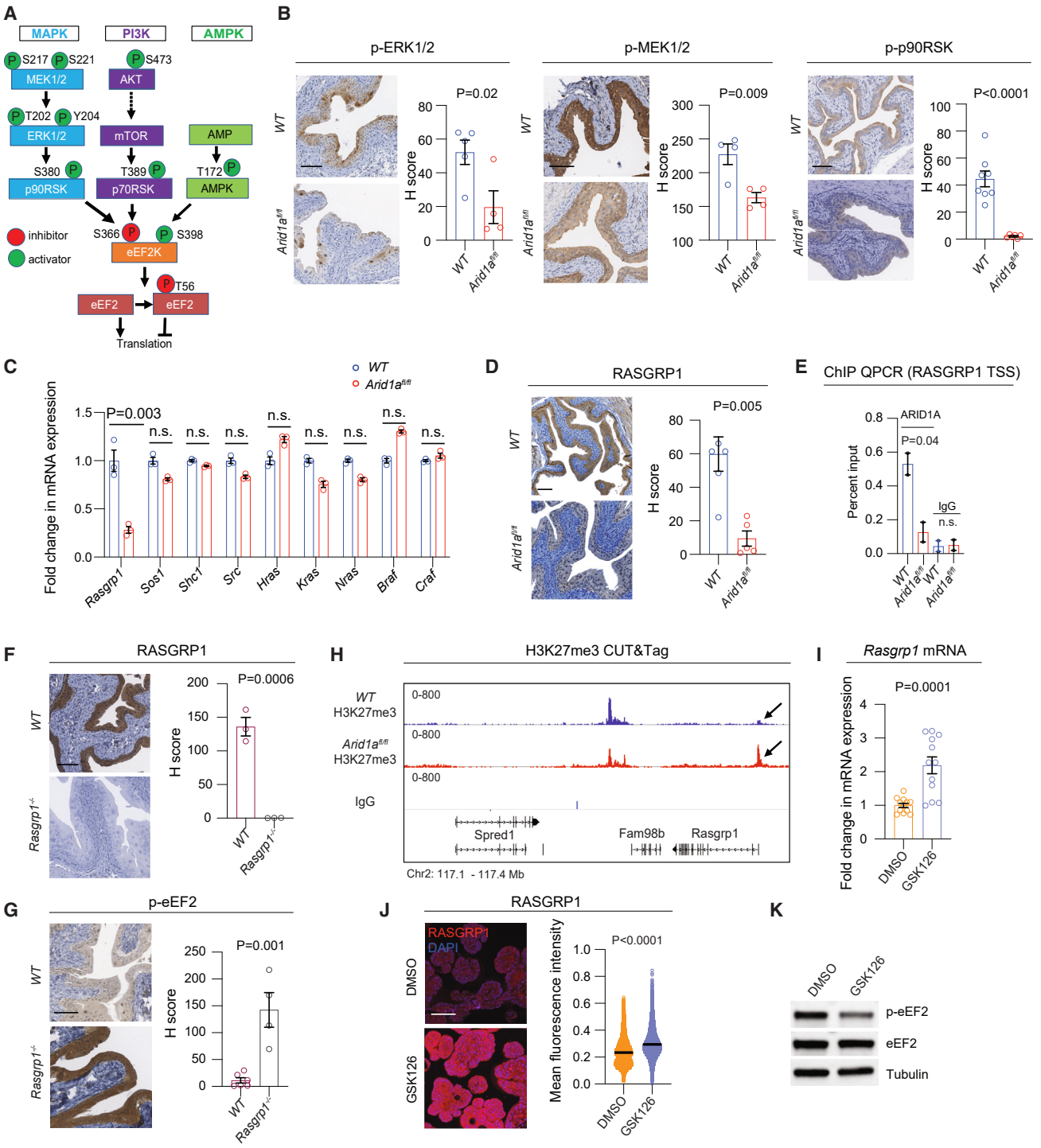

Figure 3. ARID1A regulates mRNA translation elongation through RASGRP1

(A) Schematic of upstream signaling pathways that activate (AMPK pathway) or deactivate (PI3K and MAPK pathways) eEF2K.

(B) IHC and quantification of phospho-MEK1/2, phospho-ERK1/2, and phospho-p90RSK in WT and *Arid1a*$^{fl/fl}$ urothelium. n ≥ 4/genotype. p = 0.02 (left), p = 0.009 (middle), p < 0.0001 (t test).

(C) RNA-seq mRNA expression of upstream MAPK regulators in WT and *Arid1a*$^{fl/fl}$ urothelial cells. n = 3/genotype. p = 0.003 (t test).

(D) RASGRP1 IHC and quantification in WT and *Arid1a*$^{fl/fl}$ mice. n ≥ 5/genotype. p = 0.005 (t test).

(E) *Arid1a* chromatin immunoprecipitation (ChIP) qPCR of the *Rasgrp1* promoter in WT and *Arid1a*$^{fl/fl}$ organoids. n = 2/genotype. p = 0.04 (t test).

(F and G) IHC of RASGRP1 (top) and phospho-eEF2 (T56) (bottom) in WT and *Rasgrp1*$^{-/-}$ mice. n ≥ 3/genotype. p = 0.0006 (top), p = 0.001 (bottom) (t test).

(H) H3K27me3 CUT&Tag from WT (blue) and *Arid1a*$^{fl/fl}$ (red) organoids. Black arrows, *Rasgrp1* promoter.

(legend continued on next page)

organoids (Figures 3H and S3I). Accumulation of H3K27me3 suggests that loss of ARID1A may increase polycomb repressive complex 2 (PRC2) activity at the *Rasgrp1* promoter. PRC2 marks H3K27me3 through its catalytic subunit the enhancer of zeste 2 polycomb repressive complex 2 (EZH2). To demonstrate that EZH2 catalytic activity was responsible for downregulation of *Rasgrp1*, we treated *Arid1a*$^{fl/fl}$ organoids with GSK126, a selective EZH2 inhibitor.[48] Pharmacologic inhibition of EZH2 decreased H3K27me3 on the *Rasgrp1* promoter, which restored *Rasgrp1* mRNA and protein levels in *Arid1a*$^{fl/fl}$ cells (Figures 3I, 3J, and S3J–S3L). This resulted in a decrease in eEF2 phosphorylation (Figure 3K). These findings provide a mechanism by which ARID1A controls translation elongation through modulating histone dynamics on the *Rasgrp1* promoter.

Transcriptional-translational conflict is a tumor-suppressive barrier in the urothelium

These findings raise the important question of how transcriptional-translational conflict is tumor suppressive in the urothelium. Transformation is a complex process that requires a cell to generate its own mitogenic signals, proliferate without limits, resist exogenous growth-inhibitory signals, evade apoptosis, and acquire vasculature.[49] We observed that successive passaging of primary *Arid1a*$^{fl/fl}$ urothelial organoids led to the loss of ARID1A-negative cells, which is consistent with limited replicative potential (Figure 4A). However, *Arid1a*$^{fl/fl}$;*Eef2k*$^{-/-}$ organoids remained ARID1A negative even after 9 passages, had higher clonogenic potential, and proliferated faster than *Arid1a*$^{fl/fl}$ cells (Figures 4A, S4A, and S4B). To determine if this aspect of transformation can be observed *in vivo*, we aged *Arid1a*$^{fl/fl}$;*Eef2k*$^{-/-}$ mice for 400 days. Remarkably, *Arid1a*$^{fl/fl}$;*Eef2k*$^{-/-}$, but not WT, *Arid1a*$^{fl/fl}$, or *Eef2k*$^{-/-}$ urothelium exhibited unusually thickened urothelium consistent with uncontrolled cell growth (Figures 4B and S4C). To determine if this phenotype was mediated by de-repression of conflicted mRNA, we treated *Arid1a*$^{fl/fl}$;*Eef2k*$^{-/-}$ cells with either the ODC1 inhibitor difluoromethylornithine (DFMO) or an anti-FGFR3 antibody to target ODC1 or FGFR3, respectively, and measured clonogenic growth. ODC1 and FGFR3 inhibition significantly decreased the uncontrolled growth of *Arid1a*$^{fl/fl}$;*Eef2k*$^{-/-}$ cells (Figure 4C). These findings demonstrate that de-repression of conflicted mRNAs can unmask the oncogenic properties of ARID1A loss. Furthermore, they raise the question of the role of translation restoration in tumor progression.

To test this hypothesis, we needed an experimental model where we could first increase translation elongation rates while forming tumors, then delete *Arid1a*. One of the main carcinogens found in cigarettes is N-butyl-N-(4-hydroxybutyl)nitrosamine (BBN).[50] BBN is a bladder-tropic pro-carcinogen that is metabolized into BCPN (N-butyl-N-[3-carboxypropyl]nitrosamine) and concentrated in the bladder, which causes DNA damage and bladder tumors in mice but does not cause cancer in other tissues.[51,52] We found that the process of carcinogenesis by BBN markedly increased eEF2 protein levels by 4-fold, with only a 2-fold change in eEF2 phosphorylation and no change in eEF2K levels (Figures S4D–S4F). This was associated with an increase in puromycin incorporation in bladder tumors compared with WT urothelium (Figure S4G).[53] We treated WT and non-recombined *Arid1a*$^{fl/fl}$ mice with BBN for 18 weeks to form tumors first, then dosed mice with tamoxifen to delete *Arid1a* and monitored their survival (Figure 4D). *Arid1a*$^{fl/fl}$ mice developed larger tumors, succumbed to bladder cancer at a much higher rate than WT mice (68.7% vs. 23% dead 100 days after last tamoxifen treatment, respectively), and maintained the increase in protein synthesis caused by carcinogenesis (Figures 4D, 4E, and S4H). Moreover, *Arid1a*$^{fl/fl}$ bladder tumors proliferated faster than WT tumors (Figure 4F). At a molecular level, previously conflicted mRNAs, including *Aurkb*, *Kif22*, *Odc1*, and *Ska1*, were more efficiently translated in *Arid1a*$^{fl/fl}$ tumors compared with WT tumors (Figure 4G).

Next, we sought to determine the drivers that increase protein synthesis to resolve transcriptional-translational conflict in *Arid1a*-deficient tumors. We developed a primary organoid line from a non-recombined BBN-induced *Arid1a*$^{fl/fl}$ bladder tumor (WT tumor) and used this to generate an isogenic *Arid1a*-deficient line using lentiviral Cre recombinase. We conducted pairwise RNA-seq analysis comparing normal and cancer urothelial cells in both the WT and *Arid1a*$^{fl/fl}$ backgrounds (Figure S4I). We focused our analysis on up- or downregulated mRNAs (red and blue, respectively) unique to *Arid1a* loss (Figure 4H; Table S3). We found that *Akt3*, *Fgfr1*, and *Kras* were upregulated in *Arid1a*$^{fl/fl}$ tumors. These genes have been shown to increase mRNA translation initiation and/or elongation rates.[3,33,54,55] The only protein synthesis regulator that was downregulated in *Arid1a*$^{fl/fl}$ tumors was *Eef2k* (Figure 4H; Table S3). This was associated with a significant decrease in total eEF2K and eEF2 phosphorylation in *Arid1a*$^{fl/fl}$ tumors (Figures 4I, S4J, and S4K). It has been shown that NF-kB is a negative regulator of Eef2k mRNA levels.[56] We measured a NF-kB mRNA signature in *Arid1a*$^{fl/fl}$ tumors and found that they had high NF-kB activity compared with normal *Arid1a*$^{fl/fl}$ cells, suggesting a potential mechanism for down-regulation of eEFK2 mRNA (Figure S4L).

These discoveries show that a specific threshold of protein synthesis must be achieved to overcome transcriptional-translational conflict and unlock the oncogenic potential of ARID1A loss. To determine if these findings can be observed in patients, we measured ARID1A levels and eEF2 activity levels in two independent international cohorts of muscle-invasive bladder cancer. Patient tumors with low levels of ARID1A protein were more likely to have decreased eEF2 phosphorylation, an indication of increased eEF2 activity (Figures 4J and 4K). Furthermore, ARID1A and phospho-eEF2 low patients were more likely to have high-T stage disease at diagnosis and even after neoadjuvant chemotherapy (Figures 4L and 4M). Together, our findings mechanistically show how ARID1A is a context-dependent tumor suppressor and raises the possibility that overcoming transcriptional-translational conflict through

(I) qPCR of *Rasgrp1* in *Arid1a*$^{fl/fl}$ organoids after treatment with GSK126 (12.5 μM). p = 0.0001 (t test).
(J) RASGRP1 IF in *Arid1a*$^{fl/fl}$ organoids after treatment with GSK126. n = 4/genotype, >50,000 cells/genotype. p < 0.0001 (t test).
(K) Immunoblot analysis of phospho-eEF2 and total eEF2 in *Arid1a*$^{fl/fl}$ organoids ± GSK126. Each blot is representative of three biological replicates.
n.s., not significant. Scale bar, 100 μm; mean ± SEM. Also see Figure S3.

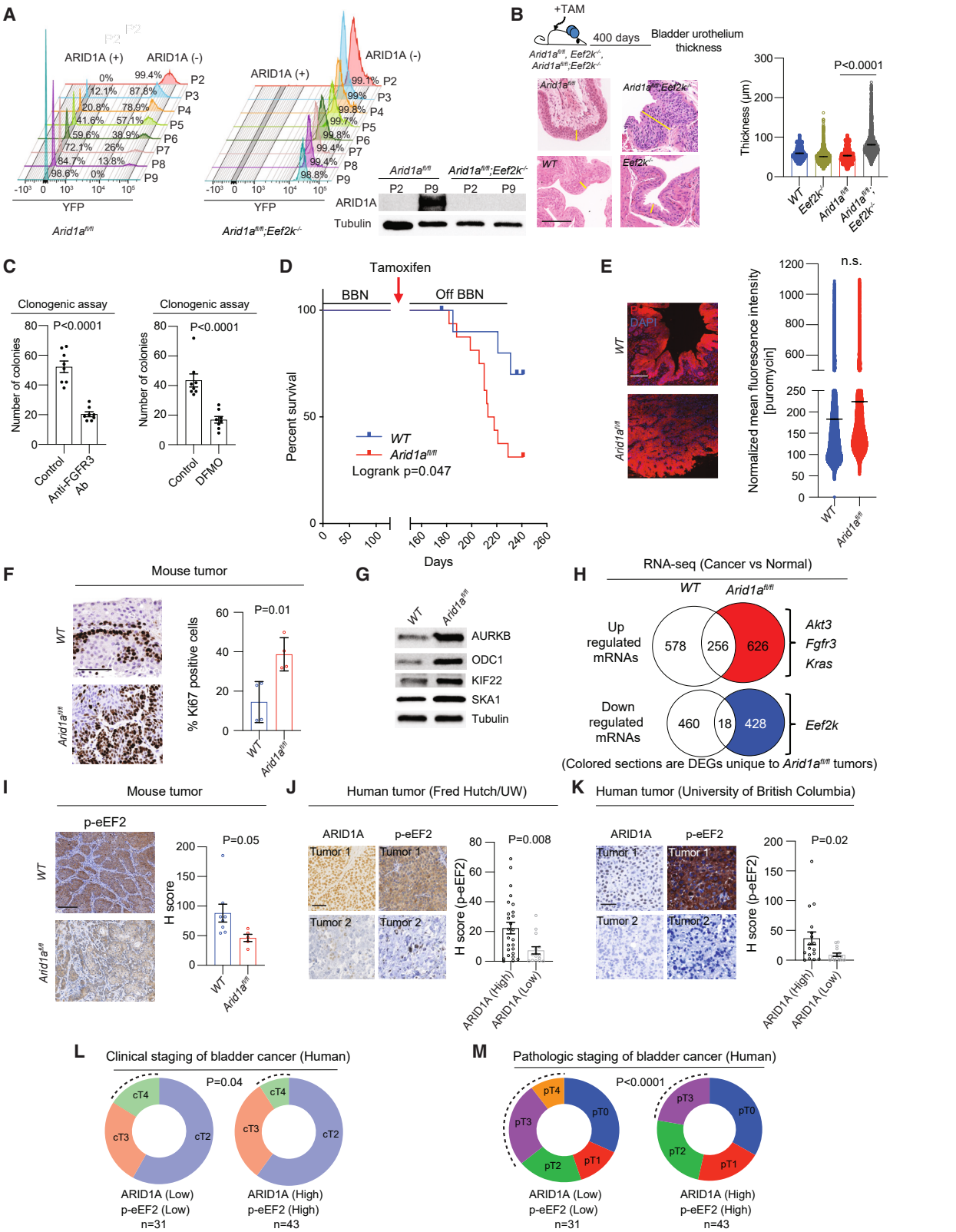

(legend on next page)

restored mRNA translation may be a linchpin to drive ARID1A-deficient tumor growth.

Drug-induced transcriptional-translational conflict is a therapeutic vulnerability in ARID1A-deficient bladder cancer

Our findings demonstrate that transcriptional-translational conflict is a barrier to cancer progression. It is possible that inducing conflict by inhibiting protein synthesis may be a strategy to target cancer growth in genotypes that have overcome this barrier to thrive. To address this hypothesis, we treated three human and murine models of bladder cancer with the translation inhibitor homoharringtonine (HHT),[57] which we chose because it is U.S. Food and Drug Administration (FDA) approved for refractory CML.[58] HHT functions by preventing ribosomes from moving past the ATG start codon, thereby stalling the initiation of elongation[57,59] (Figure 5A). First, we treated isogenic WT and *Arid1a*$^{fl/fl}$ BBN-induced cancer organoids. *Arid1a*$^{fl/fl}$ tumor organoids were sensitive to HHT at concentrations that had minimal impact on WT bladder cancer organoid growth (Figures 5B and S5A). Next, we identified 2 human ARID1A-deficient bladder cancer cell lines (HT1376 and KU1919) and 2 ARID1A-proficient bladder cancer cell lines (HT1197 and UMUC11). Interestingly, ARID1A-null cell lines were significantly more sensitive to HHT compared with cell lines that expressed ARID1A (Figures 5C and S5B).

We also conducted preclinical trials of patient-derived xenografts (PDXs) that expressed low (PDX1), medium (PDX2), or high (PDX3) ARID1A protein levels (Figure 5D), dosing HHT twice daily at a concentration physiologically achievable in human patients without any toxicity.[60,61] We observed a response that correlated with ARID1A levels. HHT decreased tumor growth by 59.3% in the ARID1A-low model, but only decreased tumor growth by 35.9% in the ARID1A-medium model (Figures 5E, 5F, and S5C). Strikingly, the ARID1A-high model was completely insensitive to HHT (Figures 5G and S5C). In addition, we found that the ARID1A-low PDX exhibited the most significant improvement in survival when treated with HHT (Figures 5H and S5D). At a cellular level, HHT increased apoptosis and decreased cell proliferation in the ARID1A-deficient but not ARID1A-proficient PDXs (Figures 5I, 5J, and S5E–S5H). These findings demonstrate that translation inhibition may reverse the gains of cancers that overcome transcriptional-translational conflict and represents a new therapeutic paradigm.

eEF2 phosphorylation leads to a collateral decrease in the translation of DNA damage response genes

Transcriptional-translational conflict is a barrier to bladder cancer pathogenesis mediated by eEF2 phosphorylation. However, the effects of slower translation elongation caused by *Arid1a* loss likely affects the protein synthesis of genes beyond the 262 upregulated oncogenic mRNAs. Indeed, analyzing mRNAs that exhibit no transcriptional difference, we found 278 additional stalled mRNAs in *Arid1a*$^{fl/fl}$ organoids (>1.35-fold change in P/S ratio, false discovery rate [FDR] < 0.05) (Figure 6A; Table S4). These stalled mRNAs also exhibited a high GC content within their coding sequences, similar to the 262 upregulated mRNAs in *Arid1a*$^{fl/fl}$ organoids (Figures S1L and S6A). Interestingly, the top Reactome pathway was DNA double-strand break repair (FDR = 5.02e-4) and included genes such as BRCA2 DNA repair-associated protein (*Brca2*), ERCC excision repair 1, endonuclease non-catalytic subunit (*Ercc1*), ERCC excision repair 2, TFIIH core complex helicase subunit (*Ercc2*), and FA complementation group C (*Fancc*) (Figure 6A). These proteins maintain genome stability enabling DNA repair and cell survival in the context of DNA damage.[62] BRCA2 plays a primary role in homology-directed repair of double-strand DNA breaks.[63] ERCC1 and ERCC2 are critical for identification, excision, and sealing of damaged DNA through nucleotide excision repair.[64] FANCC is a core component of the Fanconi anemia pathway that is required to repair interstrand crosslinks in DNA.[65] Protein levels of BRCA2, ERCC1, ERCC2, and FANCC were significantly decreased in *Arid1a*$^{fl/fl}$ organoids without concomitant changes in mRNA levels (Figures 6B, 6C, and S6B). Furthermore, genetic de-repression of eEF2 phosphorylation restored the protein levels of each of

Figure 4. Transcriptional-translational conflict is a tumor-suppressive barrier

(A) Fluorescence-activated cell sorting (FACS) analysis of *Arid1a* recombined cells (YFP$^+$) in *Arid1a*$^{fl/fl}$ and *Arid1a*$^{fl/fl}$;*Eef2k*$^{-/-}$ urothelial organoids over 9 successive passages (P2–P9). Representative ARID1A immunoblot from *Arid1a*$^{fl/fl}$ and *Arid1a*$^{fl/fl}$;*Eef2k*$^{-/-}$ urothelial organoids after two passages (P2) and 9 passages (P9).

(B) H&E (left) and urothelial thickness (right) in WT, *Eef2k*$^{-/-}$, *Arid1a*$^{fl/fl}$, and *Arid1a*$^{fl/fl}$;*Eef2k*$^{-/-}$ mice 400 days after tamoxifen. n ≥ 4/genotype. p < 0.0001 (t test).

(C) Clonogenic assay of *Arid1a*$^{fl/fl}$;*Eef2k*$^{-/-}$ urothelial cells treated with an anti-FGFR3 antibody or the ODC1 inhibitor DFMO. n = 8 biological replicates. p < 0.0001 (t test).

(D) Kaplan-Meier survival curve of WT and *Arid1a*$^{fl/fl}$ mice treated with BBN followed by tamoxifen. WT, n = 13 mice; *Arid1a*$^{fl/fl}$, n = 16 mice. p = 0.047 (Log-rank test).

(E) IF and quantification of puromycin incorporation in WT and *Arid1a*$^{fl/fl}$ mice treated with BBN followed by tamoxifen (D). n = 4/genotype, >30,000 cells/genotype.

(F) Ki67 staining and quantification in WT and *Arid1a*$^{fl/fl}$ tumors (D). n = 4/genotype. p = 0.01 (t test).

(G) Immunoblots of AURKB, KIF22, ODC1, and SKA1 in WT and *Arid1a*$^{fl/fl}$ tumors (replicate of 3).

(H) RNA-seq analysis of normal and cancer urothelial cells in WT and *Arid1a*$^{fl/fl}$ backgrounds. Upregulated (red) or downregulated (blue) mRNAs are unique to ARID1A loss (DEGs, differentially expressed genes).

(I) IHC and quantification of phospho-eEF2 (T56) in WT and *Arid1a*$^{fl/fl}$ tumors. n ≥ 5/genotype. p = 0.05 (t test).

(J) Representative images and quantification of human muscle-invasive bladder cancer (MIBC) from the University of Washington showing high and low ARID1A protein levels (left panel) and corresponding phospho-eEF2 (T56). n(ARID1A high) = 26, n(ARID1A low) = 15. p = 0.008 (t test).

(K) Representative images and quantification of MIBC obtained from the University of British Columbia showing high and low ARID1A protein levels (left panel) and corresponding phospho-eEF2 (T56). n(ARID1A high) = 17, n(ARID1A low) = 16. p = 0.02 (t test).

(L and M) Clinical staging and post-neoadjuvant chemotherapy pathologic staging of patients in (J) and (K) separated by ARID1A and p-eEF2 levels (n-low = 31, n-high = 43). p = 0.04 (L), p < 0.0001 (M) (Chi-square test).

n.s., not significant. Scale bar, 100 μm; mean ± SEM. Also see Figure S4.

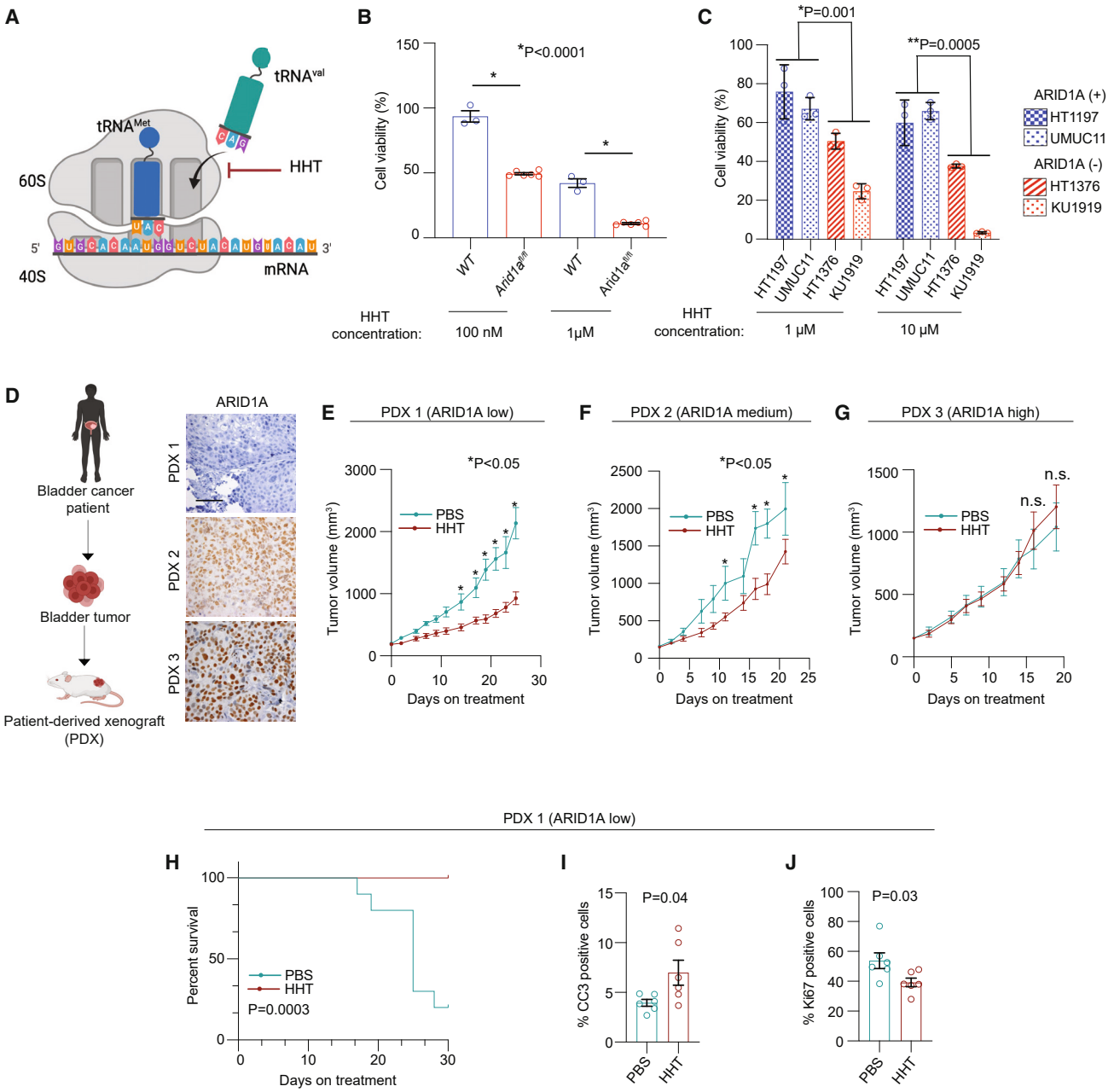

Figure 5. Pharmacologic inhibition of translation elongation initiation inhibits growth of ARID1A-deficient but not ARID1A-proficient tumors

(A) Mechanism of action of homoharringtonine (HHT).

(B) WT and *Arid1a*$^{fl/fl}$ tumor organoids cell viability after treatment with HHT (CellTiter-Glo 2.0). n ≥ 3/genotype. p < 0.0001 (t test).

(C) Cell viability of ARID1A-proficient and ARID1A-deficient human bladder cancer cell lines treated with HHT. n = 3/genotype. p = 0.001 (left), p = 0.0005 (right) (t test).

(D) Schematic of patient-derived xenograft (PDX) model generation. Representative ARID1A IHC from PDX1 (ARID1A-low), PDX2 (ARID1A-medium), and PDX3 (ARID1A-high) tumor tissues.

(E–G) Tumor growth rate in PDX1, PDX2, and PDX3 models treated with HHT (0.7 mg/kg; twice/day). n ≥ 10/treatment arm, p < 0.05.

(H) HHT or vehicle (PBS) PDX1 Kaplan-Meier survival curve. n = 10/arm. p = 0.0003 (log-rank test).

(I) Percentage CC3-positive cells from the PDX1 group treated with HHT or vehicle (PBS). n = 6/arm. p = 0.04 (t test).

(J) Percentage Ki67-positive cells from the PDX1 group treated with HHT or vehicle (PBS). n = 6/treatment arm. p = 0.03 (t test).

n.s., not significant. Mean ± SEM. Also see Figure S5.

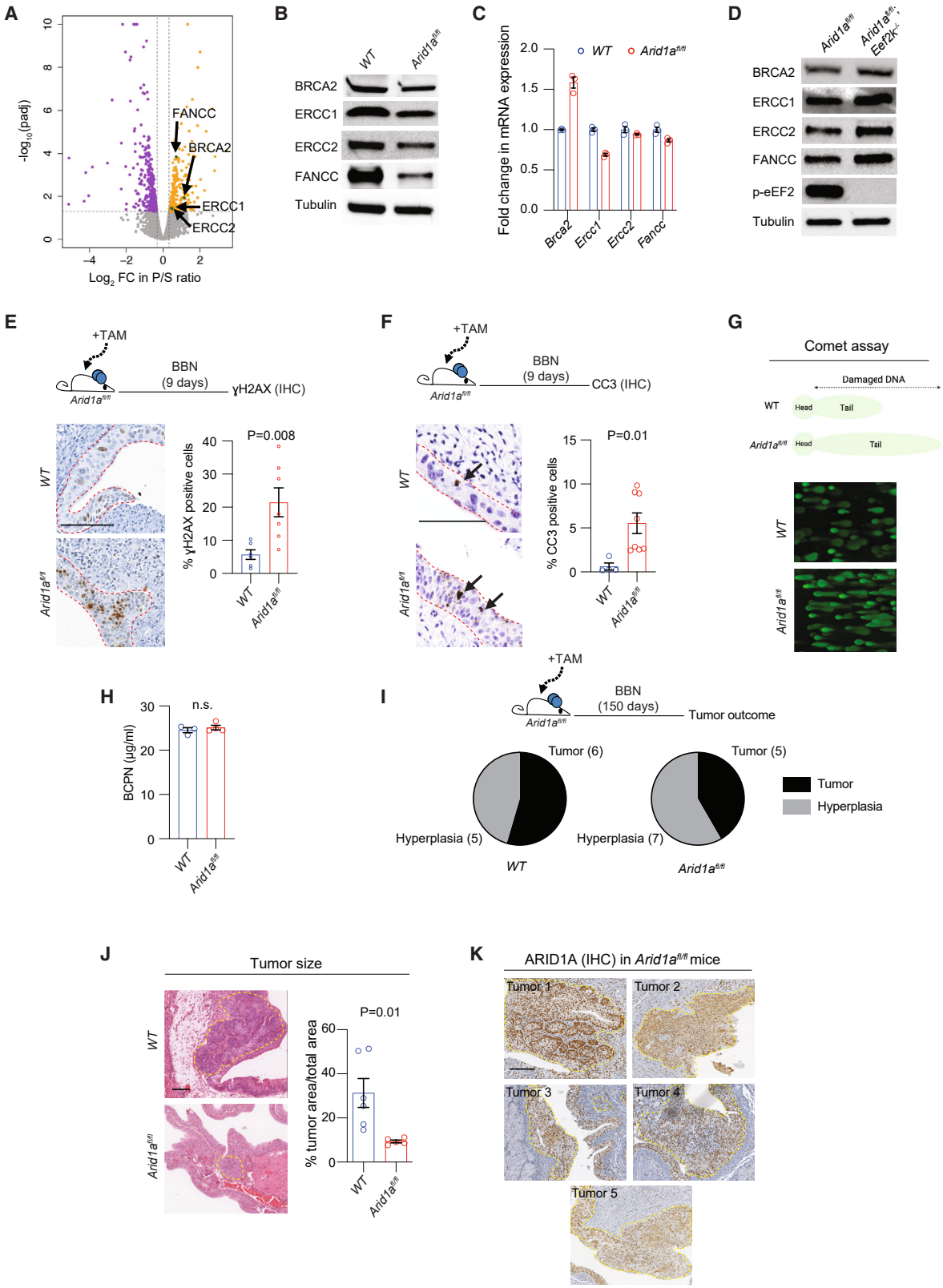

Figure 6. ARID1A loss leads to a decrease in the translation of DNA damage response mRNAs

(A) Volcano plot showing 278 translationally stalled mRNAs (orange dots, increased P/S ratio), which include *Brca2*, *Ercc1*, *Ercc2*, and *Fancc* (FDR < 0.05).
(B and C) Protein (replicate of 2) and mRNA (replicate of 3) levels of DNA damage response genes in WT and *Arid1a*$^{fl/fl}$ urothelial cells.

(legend continued on next page)

these genes (Figure 6D). Therefore, transcriptional-translational conflict leads to the collateral decrease of gene networks critical for DNA damage repair.

To determine if the decreased protein synthesis of DNA damage response genes creates a vulnerability to DNA damage in *Arid1a*-deficient urothelium, we treated WT and *Arid1a*$^{fl/fl}$ mice with BBN for 9 days and measured γH2AX foci (a marker for double-stranded DNA breaks) and cleaved caspase-3 (CC3; a marker for apoptosis). *Arid1a*-deficient mice exhibited a significant increase in urothelial γH2AX and CC3 (Figures 6E and 6F). This was associated with increased DNA damage, as measured using the comet assay (Figure 6G). Mass spectrometry for BCPN in WT and *Arid1a*$^{fl/fl}$ mouse urine showed no difference in carcinogen exposure (Figure 6H). These findings suggest that *Arid1a*$^{fl/fl}$ cells may exhibit impaired transformation because of an inability to efficiently repair damaged DNA. To test this concept, WT and *Arid1a*-deficient mice were dosed with BBN for 150 days. Although both WT and *Arid1a*$^{fl/fl}$ mice developed the same number of tumors, *Arid1a*$^{fl/fl}$ tumors were smaller compared with their WT counterparts (Figures 6I and 6J). Given the mosaic nature of the *Arid1a*$^{fl/fl}$ model (Figure S1A) we reasoned that if loss of ARID1A is an impediment toward transformation, then the WT urothelium should more readily form tumors. Indeed, all tumors in *Arid1a*$^{fl/fl}$ mice still expressed ARID1A (Figure 6K). Thus, ARID1A is necessary to enable the survival of BBN-treated urothelium raising the question of the role of translation elongation in this process.

eEF2 activity is necessary for carcinogenesis in the context of ARID1A loss

ARID1A directly interacts with ataxia telangiectasia and RAD3-related protein (ATR) to promote double-strand break end resection and ATR activation to maintain chromosomal stability in response to radiation.[11] Our data suggest that mRNA-specific translation elongation downstream of ARID1A may also promote DNA damage repair and cell survival. To determine if the decrease in translation elongation which occurs upon ARID1A loss is responsible for the impaired DDR independent of ARID1A's role as an ATR interactor, we treated *Arid1a*$^{fl/fl}$ and *Arid1a*$^{fl/fl}$;*Eef2k*$^{-/-}$ mice with BBN for 9 days. We found that genetic restoration of translation elongation, which restored BRCA2, ERCC1, ERCC2, and FANCC protein abundance, was sufficient to decrease DNA damage and apoptosis in *Arid1a*$^{fl/fl}$;*Eef2k*$^{-/-}$ mice (Figures 6D, 7A, and 7B). Carcinogen exposure in both mouse models was equivalent (Figure S7A). To determine if this rescue was mediated by the catalytic activity of eEF2K, we pre-treated *Arid1a*$^{fl/fl}$ mice with A-484954 before a 9-day course of BBN. Like the genetic model, inhibition of eEF2K activity markedly decreased DNA damage and apoptosis (Figures 7C, 7D, and S7B).

These short-term studies raise the possibility that mRNA-specific impairments in translation elongation form a protective barrier that prevent *Arid1a*-deficient cells from carcinogen-mediated transformation. To directly address this question, *Arid1a*$^{fl/fl}$ and *Arid1a*$^{fl/fl}$;*Eef2k*$^{-/-}$ mice were treated with BBN for 150 days. *Arid1a*$^{fl/fl}$;*Eef2k*$^{-/-}$ mice formed significantly larger bladder tumors compared with *Arid1a*$^{fl/fl}$ mice (Figures 7E and S7C). Remarkably, unlike all tumors in *Arid1a*$^{fl/fl}$ mice which continue to express ARID1A protein, only 1 of 7 *Arid1a*$^{fl/fl}$;*Eef2k*$^{-/-}$ tumors was positive for ARID1A (Figures 6K, 7F, and 7G). As such, restoring translation elongation and mRNA-specific translation is sufficient to drive carcinogenesis and the formation of *Arid1a*-deficient tumors.

DISCUSSION

Here we demonstrate that a tumor suppressor can function as a positive regulator of translation elongation. This has historical precedence because major tumor suppressors have been shown to negatively, but not positively regulate the protein-synthetic capacity of cells. For example, TP53 binds to and inhibits the rRNA methyl-transferase fibrillarin which prevents IRES-mediated translation of cancer genes.[1] Loss of PTEN within prostate epithelium promotes cancer progression through hyperactivation of the mTOR-eIF4F signaling pathway and translation of pro-metastasis mRNAs.[2] APC loss leads to intestinal tumorigenesis driven by enhanced translation elongation of cyclin D mRNA.[3] Contrary to these tumor suppressors, we show that ARID1A is necessary for the maintenance of translation elongation through eEF2 (Figure S7D). Therefore, loss of ARID1A has significant negative implications for the ability of upregulated proliferation and oncogenic mRNA networks to be synthesized into proteins. This conflict between transcription and translation forms a functional barrier to uncontrolled cell growth and cancer progression, which we propose is a source of oncogenic stress that occurs when chromatin remodeling is deregulated in urothelium.

This concept has important parallels with other major oncogenic signaling pathways. For example, it has been shown that loss of the tumor suppressor PTEN can upregulate TP53 levels which promotes cellular senescence and prevents the formation of lethal prostate cancer. However, combined loss of PTEN and TP53 can overcome this barrier leading to uninhibited tumor growth.[66] This is also true for oncogenes such as MYC and PIK3CA. MYC which is commonly amplified in human malignancies causes apoptosis in the context of overexpression in normal cells.[67,68]

(D) Protein levels of DNA damage response genes in *Arid1a*$^{fl/fl}$ and *Arid1a*$^{fl/fl}$;*Eef2k*$^{-/-}$ urothelial cells (replicate of 3).
(E and F) γH2AX or CC3 staining and quantification in WT and *Arid1a*$^{fl/fl}$ mice after tamoxifen administration followed by 9 days of BBN treatment. Urothelium is marked with red dotted lines. n ≥ 4/genotype. p = 0.008 (E), p = 0.01 (F) (t test).
(G) Representative comet assay showing increased DNA damage (tail length) in *Arid1a*$^{fl/fl}$ organoids compared with WT organoids treated with BCPN.
(H) Mass spectrometry measurements of urine BCPN in WT and *Arid1a*$^{fl/fl}$ mice after 9 days of BBN treatment (n ≥ 3/genotype).
(I) Pie chart showing tumor outcome in WT and *Arid1a*$^{fl/fl}$ mice treated with BBN for 150 days after ARID1A deletion (WT, n = 11; *Arid1a*$^{fl/fl}$, n = 12).
(J) H&E staining of tumors from WT and *Arid1a*$^{fl/fl}$ mice after 150 days of BBN treatment. Tumor area is marked with yellow dotted lines. WT, n = 6 tumors; *Arid1a*$^{fl/fl}$, n = 5 tumors. p = 0.01 (t test).
(K) ARID1A IHC of *Arid1a*$^{fl/fl}$ tumors after tamoxifen followed by 150 days of BBN treatment (I). Tumor area is marked with yellow dotted lines.
n.s., not significant. Scale bar, 100 μm; mean ± SEM. Also see Figure S6.

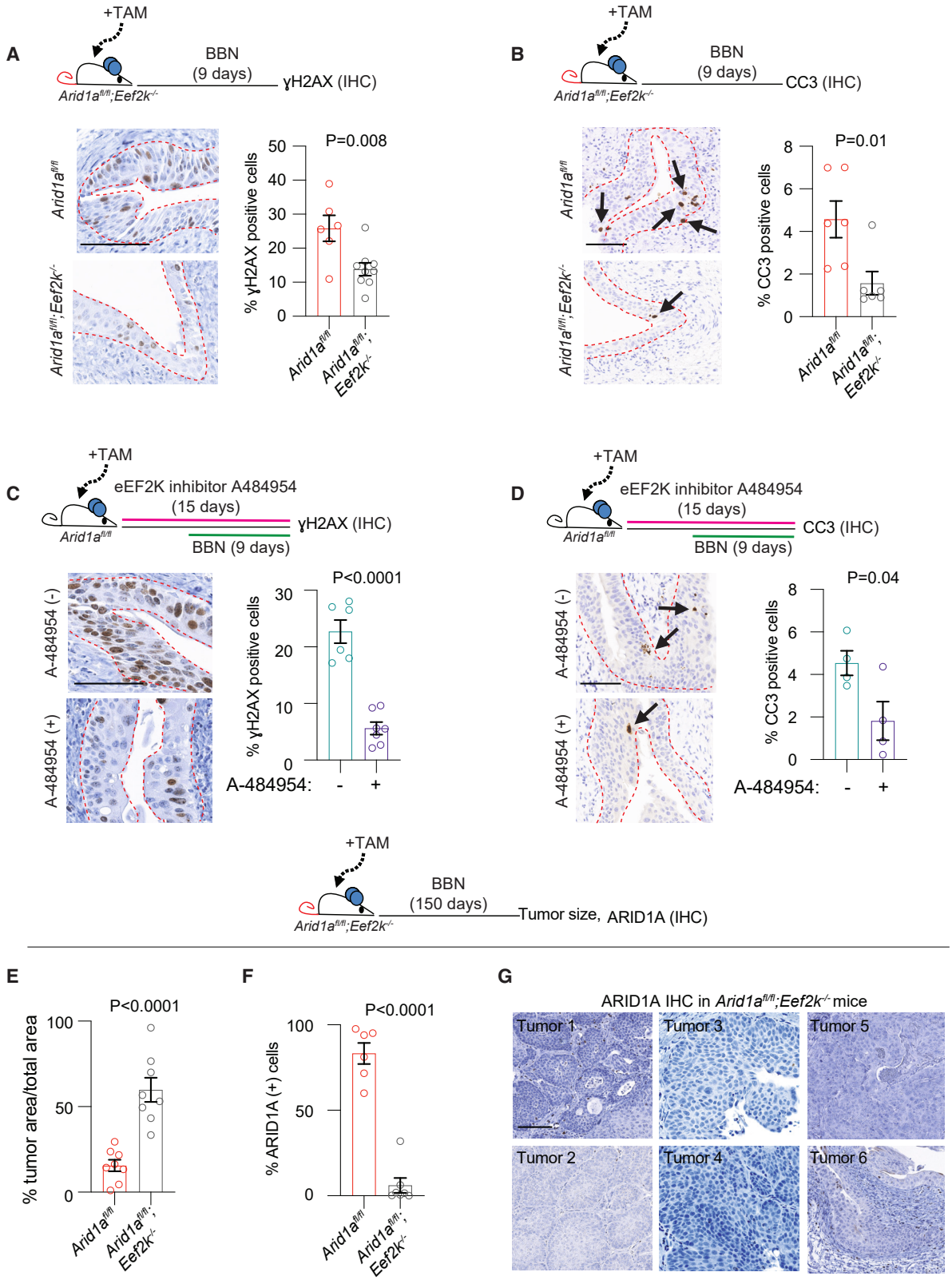

Figure 7. Restoration of translation elongation is necessary to enable carcinogenesis in ARID1A-deficient urothelium

(A and B) γH2AX and CC3 staining and quantification in *Arid1a*$^{fl/fl}$ and *Arid1a*$^{fl/fl}$;*Eef2k*$^{-/-}$ mouse urothelium (outlined in red) after tamoxifen administration followed by 9 days of BBN treatment. n ≥ 6/genotype. p = 0.008 (A), p = 0.01 (B) (t test).

(legend continued on next page)

This is mediated through enhanced expression of the apoptosis regulator BIM.[69] Importantly co-expression of MYC and the anti-apoptotic and inhibitor of BIM, BCL-2, leads to a significant acceleration in tumorigenesis.[70] Activated PIK3CA causes cellular differentiation in epidermal progenitors which is mediated by the AKT substrate SH3RF1. This leads to terminal differentiation of epidermal cells that possess activating mutations of PIK3CA and prevents oncogenic clonal expansion.[71] In line with these oncogenic stress pathways, our data show that ARID1A loss leads to a significant reduction in eEF2 activity which promotes a conflict between the expression of oncogenic genes and their subsequent translation (Figure S7D). Restoration of translation elongation enabling gene expression parity is sufficient to unleash the oncogenic properties of ARID1A deficiency leading to uncontrolled cell growth and tumor progression.

The relationship between ARID1A and protein synthesis may be a common theme in enabling transformation or cancer progression in the context of ARID1A loss. ARID1A deficiency by itself does not drive transformation in murine ovary, liver, lung, or pancreas, and human gastric organoids.[5–7,72–74] However, it has been shown in these tissues that co-deletion of the tumor suppressor PTEN,[7] overexpression of the oncogene MYC,[5] or expression of oncogenic KRAS or PIK3CA[6,72,73] along with ARID1A loss can drive tumorigenesis and cancer progression. All of these oncogenic signaling pathways that synergize with ARID1A loss are regulators of protein synthesis.[75] Therefore, gaining the ability to synthesize proteins efficiently is a key parameter for enabling the oncogenic properties of ARID1A loss. Our work reveals that ARID1A deficiency leads to a selective decrease in the translation of key oncogenic factors and DNA damage repair machinery. It remains to be determined if this is also true in other normal tissues. To this end, we have observed that ARID1A loss leads to a decrease in *de novo* protein synthesis within human prostate epithelial cells and murine bone marrow derived stroma (Figures S7E and S7F).

We have also identified a therapeutic vulnerability unique to ARID1A-deficient tumors. Given that rescue of translation elongation is needed to drive ARID1A-deficient tumor progression, we reasoned that this may provide a therapeutic window using an FDA approved translation inhibitor. Using 3 model systems, we found that ARID1A-deficient but not proficient cancers are exquisitely sensitive to translation inhibition. It has also been shown that SWI/SNF defective cancer cell lines and rhabdoid tumors are also sensitive to PI3K pathway inhibitors or HHT.[76,77] These finding demonstrate how ARID1A deficiency creates a synthetic lethal relationship with mRNA translation which can be targeted to inhibit tumor growth. Given that multiple components of the SWI/SNF complex are mutated in various cancers,[9] our findings raise the possibility that targeting the translation apparatus may represent a new precision medicine paradigm applicable to a wide spectrum of human malignancies.

STAR★METHODS

Detailed methods are provided in the online version of this paper and include the following:

- KEY RESOURCES TABLE
- RESOURCE AVAILABILITY
  - Lead contact
  - Materials availability
  - Data and code availability
- EXPERIMENTAL MODELS AND SUBJECT DETAILS
  - Mice
  - Cell culture
  - Organoid culture
- METHOD DETAILS
  - ARID1A re-expression
  - Rasgrp1 re-expression
  - Urine BCPN analysis
  - Immunoblot analysis
  - Mouse genotyping
  - Hematoxylin and eosin staining (H&E), immunohistochemistry (IHC), immunofluorescence (IF)
  - ChIP qPCR
  - *In vivo* and *in vitro* puromycin incorporation assay
  - RNA sequencing and polysome-bound RNA sequencing
  - *In vitro* [^{35}S]-methionine labeling assay
  - Cell viability assay
  - siRNA knockdown
  - Polysome profiling
  - Ribosome half-transit time
  - TMT mass spectrometry
  - Preclinical trials
  - CUT&Tag chromatin profiling
  - Flow cytometry
  - Cell cycle analysis
  - Comet assay
  - Clonogenic assay
  - Organoid embedding and staining
  - Drug administration
- QUANTIFICATION AND STATISTICAL ANALYSIS
  - RNA-sequencing and polysome sequencing analysis
  - CUT&Tag data analysis
  - TMT mass spectrometry data analysis
  - Ribosome half-transit time data analysis
  - %GC content in coding sequence analysis

(C and D) γH2AX and CC3 staining and quantification in *Arid1a*$^{fl/fl}$ mouse urothelium (outlined in red) after tamoxifen administration and pre-treatment with A-484954 followed by a 9-day BBN treatment. n ≥ 4/arm. p < 0.0001 (C), p = 0.04 (D) (t test).
(E) Tumor size after tamoxifen followed by 150 days of BBN treatment in *Arid1a*$^{fl/fl}$ and *Arid1a*$^{fl/fl}$;*Eef2k*$^{-/-}$ mice. n ≥ 6/genotype. p < 0.0001 (t test).
(F) Percentage ARID1A (+) cells in *Arid1a*$^{fl/fl}$ and *Arid1a*$^{fl/fl}$;*Eef2k*$^{-/-}$ mice after tamoxifen followed by 150 days of BBN treatment. n ≥ 6/genotype. p < 0.0001 (t test).
(G) ARID1A IHC of *Arid1a*$^{fl/fl}$;*Eef2k*$^{-/-}$ tumors after tamoxifen followed by 150 days of BBN treatment. This demonstrates the presence of ARID1A-null tumors compared with Figure 6K.
Scale bar, 100 μm; mean ± SEM. Also see Figure S7.

SUPPLEMENTAL INFORMATION

Supplemental information can be found online at https://doi.org/10.1016/j.ccell.2023.03.021.

ACKNOWLEDGMENTS

We thank the patients who contributed to this study. This work was supported by the Kleberg Foundation, NIH grants R01 CA276308, R37 CA230617, R01 GM135362, and P30 CA015704, a Burroughs Wellcome Fund Career Award of Medicine Scientists (1012314.02), and grants from the Emerson Collective (691630), Seattle Translational Tumor Research, and Nancy & Dick Bernheimer, Matthews Family, Stinchcomb Family, and Thomas & Patricia Wright Memorial Funds to A.C.H. This research was also supported by the Shared Resources of the FHCC/UW (P30 CA015704 and S10 OD028685), NIH grants R01 CA187318 (J.P.R.), P01 AI091580 (J.P.R.), and the Mark Foundation For Cancer Research (P.D.). H.-M.L. is supported by U.S. Department of Defense (DOD) grant W81XWH-19-1-0624. S.J. is supported by DOD grant W81XWH-19-1-0658. S. Brahma is supported by NIH grant K99-GM138920. S. Blinka is supported by NIH grant T32-CA009515.

AUTHOR CONTRIBUTIONS

Conceptualization, S.J. and A.C.H.; Investigation, S.J., S. Brahma, C.L.W., P.H., S. Blinka, R.H., J.L.H., Y.L., S.A., L.-J.W., P.D., E.S., M.C.H., and A.R.S.; Writing – Original Draft, S.J. and A.C.H.; Writing – Review & Editing, S.J., A.C.H., R.B.M., J.K.L., P.G., J.L.W., H.-M.L., P.C.V., J.P.R., A.G.R., and S.H.; Funding Acquisition, A.C.H.; Resources, R.B.M., J.K.L., P.G., J.L.W., H.-M.L., P.C.V., J.P.R., A.G.R., and S.H.

DECLARATION OF INTERESTS

The authors declare no competing interests.

Received: July 27, 2022
Revised: January 31, 2023
Accepted: March 24, 2023
Published: April 20, 2023

REFERENCES

1. Marcel, V., Ghayad, S.E., Belin, S., Therizols, G., Morel, A.P., Solano-Gonzàlez, E., Vendrell, J.A., Hacot, S., Mertani, H.C., Albaret, M.A., et al. (2013). p53 acts as a safeguard of translational control by regulating fibrillarin and rRNA methylation in cancer. Cancer Cell *24*, 318–330. https://doi.org/10.1016/j.ccr.2013.08.013.
2. Hsieh, A.C., Liu, Y., Edlind, M.P., Ingolia, N.T., Janes, M.R., Sher, A., Shi, E.Y., Stumpf, C.R., Christensen, C., Bonham, M.J., et al. (2012). The translational landscape of mTOR signalling steers cancer initiation and metastasis. Nature *485*, 55–61. https://doi.org/10.1038/nature10912.
3. Faller, W.J., Jackson, T.J., Knight, J.R., Ridgway, R.A., Jamieson, T., Karim, S.A., Jones, C., Radulescu, S., Huels, D.J., Myant, K.B., et al. (2015). mTORC1-mediated translational elongation limits intestinal tumour initiation and growth. Nature *517*, 497–500. https://doi.org/10.1038/nature13896.
4. Yang, H.S., Jansen, A.P., Komar, A.A., Zheng, X., Merrick, W.C., Costes, S., Lockett, S.J., Sonenberg, N., and Colburn, N.H. (2003). The transformation suppressor Pdcd4 is a novel eukaryotic translation initiation factor 4A binding protein that inhibits translation. Mol. Cell Biol. *23*, 26–37. https://doi.org/10.1128/mcb.23.1.26-37.2003.
5. Sun, X., Wang, S.C., Wei, Y., Luo, X., Jia, Y., Li, L., Gopal, P., Zhu, M., Nassour, I., Chuang, J.C., et al. (2017). Arid1a has context-dependent oncogenic and tumor suppressor functions in liver cancer. Cancer Cell *32*, 574–589.e6. https://doi.org/10.1016/j.ccell.2017.10.007.
6. Chandler, R.L., Damrauer, J.S., Raab, J.R., Schisler, J.C., Wilkerson, M.D., Didion, J.P., Starmer, J., Serber, D., Yee, D., Xiong, J., et al. (2015). Coexistent ARID1A-PIK3CA mutations promote ovarian clear-cell tumorigenesis through pro-tumorigenic inflammatory cytokine signalling. Nat. Commun. *6*, 6118. https://doi.org/10.1038/ncomms7118.
7. Guan, B., Rahmanto, Y.S., Wu, R.C., Wang, Y., Wang, Z., Wang, T.L., and Shih, I.M. (2014). Roles of deletion of Arid1a, a tumor suppressor, in mouse ovarian tumorigenesis. J. Natl. Cancer Inst. *106*, dju146. https://doi.org/10.1093/jnci/dju146.
8. ICGC/TCGA Pan-Cancer Analysis of Whole Genomes Consortium (2020). Pan-cancer analysis of whole genomes. Nature *578*, 82–93. https://doi.org/10.1038/s41586-020-1969-6.
9. Kadoch, C., and Crabtree, G.R. (2015). Mammalian SWI/SNF chromatin remodeling complexes and cancer: mechanistic insights gained from human genomics. Sci. Adv. *1*, e1500447. https://doi.org/10.1126/sciadv.1500447.
10. Centore, R.C., Sandoval, G.J., Soares, L.M.M., Kadoch, C., and Chan, H.M. (2020). Mammalian SWI/SNF chromatin remodeling complexes: emerging mechanisms and therapeutic strategies. Trends Genet. *36*, 936–950. https://doi.org/10.1016/j.tig.2020.07.011.
11. Shen, J., Peng, Y., Wei, L., Zhang, W., Yang, L., Lan, L., Kapoor, P., Ju, Z., Mo, Q., Shih, I.M., et al. (2015). ARID1A deficiency impairs the DNA damage checkpoint and sensitizes cells to PARP inhibitors. Cancer Discov. *5*, 752–767. https://doi.org/10.1158/2159-8290.CD-14-0849.
12. Dykhuizen, E.C., Hargreaves, D.C., Miller, E.L., Cui, K., Korshunov, A., Kool, M., Pfister, S., Cho, Y.J., Zhao, K., and Crabtree, G.R. (2013). BAF complexes facilitate decatenation of DNA by topoisomerase IIalpha. Nature *497*, 624–627. https://doi.org/10.1038/nature12146.
13. Siegel, R.L., Miller, K.D., Fuchs, H.E., and Jemal, A. (2021). Cancer statistics, 2021. CA. Cancer J. Clin. *71*, 7–33. https://doi.org/10.3322/caac.21654.
14. Robertson, A.G., Kim, J., Al-Ahmadie, H., Bellmunt, J., Guo, G., Cherniack, A.D., Hinoue, T., Laird, P.W., Hoadley, K.A., Akbani, R., et al. (2017). Comprehensive molecular characterization of muscle-invasive bladder cancer. Cell *171*, 540–556.e25. https://doi.org/10.1016/j.cell.2017.09.007.
15. Winters, B.R., De Sarkar, N., Arora, S., Bolouri, H., Jana, S., Vakar-Lopez, F., Cheng, H.H., Schweizer, M.T., Yu, E.Y., Grivas, P., et al. (2019). Genomic distinctions between metastatic lower and upper tract urothelial carcinoma revealed through rapid autopsy. JCI Insight *5*, e128728. https://doi.org/10.1172/jci.insight.128728.
16. Faltas, B.M., Prandi, D., Tagawa, S.T., Molina, A.M., Nanus, D.M., Sternberg, C., Rosenberg, J., Mosquera, J.M., Robinson, B., Elemento, O., et al. (2016). Clonal evolution of chemotherapy-resistant urothelial carcinoma. Nat. Genet. *48*, 1490–1499. https://doi.org/10.1038/ng.3692.
17. Van Batavia, J., Yamany, T., Molotkov, A., Dan, H., Mansukhani, M., Batourina, E., Schneider, K., Oyon, D., Dunlop, M., Wu, X.R., et al. (2014). Bladder cancers arise from distinct urothelial sub-populations. Nat. Cell Biol. *16*, 981–985. https://doi.org/10.1038/ncb3038.
18. Shin, K., Lim, A., Odegaard, J.I., Honeycutt, J.D., Kawano, S., Hsieh, M.H., and Beachy, P.A. (2014). Cellular origin of bladder neoplasia and tissue dynamics of its progression to invasive carcinoma. Nat. Cell Biol. *16*, 469–478. https://doi.org/10.1038/ncb2956.
19. Chiu, Y.F., Wu, C.C., Kuo, M.H., Miao, C.C., Zheng, M.Y., Chen, P.Y., Lin, S.C., Chang, J.L., Wang, Y.H., and Chou, Y.T. (2020). Critical role of SOX2-IGF2 signaling in aggressiveness of bladder cancer. Sci. Rep. *10*, 8261. https://doi.org/10.1038/s41598-020-65006-z.
20. Lin, H., Huang, Y.S., Fustin, J.M., Doi, M., Chen, H., Lai, H.H., Lin, S.H., Lee, Y.L., King, P.C., Hou, H.S., et al. (2021). Hyperpolyploidization of hepatocyte initiates preneoplastic lesion formation in the liver. Nat. Commun. *12*, 645. https://doi.org/10.1038/s41467-020-20572-8.
21. Erichsen, L., Seifert, H.H., Schulz, W.A., Hoffmann, M.J., Niegisch, G., Araúzo-Bravo, M.J., Bendhack, M.L., Poyet, C., Hermanns, T., Beermann, A., et al. (2020). Basic hallmarks of urothelial cancer unleashed in primary uroepithelium by interference with the epigenetic master regulator ODC1. Sci. Rep. *10*, 3808. https://doi.org/10.1038/s41598-020-60796-8.

22. Foth, M., Ismail, N.F.B., Kung, J.S.C., Tomlinson, D., Knowles, M.A., Eriksson, P., Sjödahl, G., Salmond, J.M., Sansom, O.J., and Iwata, T. (2018). FGFR3 mutation increases bladder tumourigenesis by suppressing acute inflammation. J. Pathol. *246*, 331–343. https://doi.org/10.1002/path.5143.

23. Nguyen, H.G., Makitalo, M., Yang, D., Chinnappan, D., St Hilaire, C., and Ravid, K. (2009). Deregulated Aurora-B induced tetraploidy promotes tumorigenesis. FASEB J *23*, 2741–2748. https://doi.org/10.1096/fj.09-130963.

24. Pravtcheva, D.D., and Wise, T.L. (1998). Metastasizing mammary carcinomas in H19 enhancers-Igf2 transgenic mice. J. Exp. Zool. *281*, 43–57.

25. Zingone, A., Cultraro, C.M., Shin, D.M., Bean, C.M., Morse, H.C., 3rd, Janz, S., and Kuehl, W.M. (2010). Ectopic expression of wild-type FGFR3 cooperates with MYC to accelerate development of B-cell lineage neoplasms. Leukemia *24*, 1171–1178. https://doi.org/10.1038/leu.2010.50.

26. Liu, Y., Horn, J.L., Banda, K., Goodman, A.Z., Lim, Y., Jana, S., Arora, S., Germanos, A.A., Wen, L., Hardin, W.R., et al. (2019). The androgen receptor regulates a druggable translational regulon in advanced prostate cancer. Sci. Transl. Med. *11*, eaaw4993. https://doi.org/10.1126/scitranslmed.aaw4993.

27. Trizzino, M., Barbieri, E., Petracovici, A., Wu, S., Welsh, S.A., Owens, T.A., Licciulli, S., Zhang, R., and Gardini, A. (2018). The tumor suppressor ARID1A controls global transcription via pausing of RNA polymerase II. Cell Rep. *23*, 3933–3945. https://doi.org/10.1016/j.celrep.2018.05.097.

28. Jiang, L., Schlesinger, F., Davis, C.A., Zhang, Y., Li, R., Salit, M., Gingeras, T.R., and Oliver, B. (2011). Synthetic spike-in standards for RNA-seq experiments. Genome Res. *21*, 1543–1551. https://doi.org/10.1101/gr.121095.111.

29. Lim, Y., Arora, S., Schuster, S.L., Corey, L., Fitzgibbon, M., Wladyka, C.L., Wu, X., Coleman, I.M., Delrow, J.J., Corey, E., et al. (2021). Multiplexed functional genomic analysis of 5' untranslated region mutations across the spectrum of prostate cancer. Nat. Commun. *12*, 4217. https://doi.org/10.1038/s41467-021-24445-6.

30. Nielsen, P.J., and McConkey, E.H. (1980). Evidence for control of protein synthesis in HeLa cells via the elongation rate. J. Cell. Physiol. *104*, 269–281. https://doi.org/10.1002/jcp.1041040302.

31. Bentele, K., Saffert, P., Rauscher, R., Ignatova, Z., and Blüthgen, N. (2013). Efficient translation initiation dictates codon usage at gene start. Mol. Syst. Biol. *9*, 675. https://doi.org/10.1038/msb.2013.32.

32. Truitt, M.L., and Ruggero, D. (2016). New frontiers in translational control of the cancer genome. Nat. Rev. Cancer *16*, 288–304. https://doi.org/10.1038/nrc.2016.27.

33. Hsieh, A.C., Costa, M., Zollo, O., Davis, C., Feldman, M.E., Testa, J.R., Meyuhas, O., Shokat, K.M., and Ruggero, D. (2010). Genetic dissection of the oncogenic mTOR pathway reveals druggable addiction to translational control via 4EBP-eIF4E. Cancer Cell *17*, 249–261. https://doi.org/10.1016/j.ccr.2010.01.021.

34. Nguyen, H.G., Conn, C.S., Kye, Y., Xue, L., Forester, C.M., Cowan, J.E., Hsieh, A.C., Cunningham, J.T., Truillet, C., Tameire, F., et al. (2018). Development of a stress response therapy targeting aggressive prostate cancer. Sci. Transl. Med. *10*, eaar2036. https://doi.org/10.1126/scitranslmed.aar2036.

35. Ryazanov, A.G., Shestakova, E.A., and Natapov, P.G. (1988). Phosphorylation of elongation factor 2 by EF-2 kinase affects rate of translation. Nature *334*, 170–173. https://doi.org/10.1038/334170a0.

36. Redpath, N.T., and Proud, C.G. (1993). Purification and phosphorylation of elongation factor-2 kinase from rabbit reticulocytes. Eur. J. Biochem. *212*, 511–520. https://doi.org/10.1111/j.1432-1033.1993.tb17688.x.

37. Leprivier, G., Remke, M., Rotblat, B., Dubuc, A., Mateo, A.R.F., Kool, M., Agnihotri, S., El-Naggar, A., Yu, B., Somasekharan, S.P., et al. (2013). The eEF2 kinase confers resistance to nutrient deprivation by blocking translation elongation. Cell *153*, 1064–1079. https://doi.org/10.1016/j.cell.2013.04.055.

38. Chen, Z., Gopalakrishnan, S.M., Bui, M.H., Soni, N.B., Warrior, U., Johnson, E.F., Donnelly, J.B., and Glaser, K.B. (2011). 1-Benzyl-3-cetyl-2-methylimidazolium iodide (NH125) induces phosphorylation of eukaryotic elongation factor-2 (eEF2): a cautionary note on the anticancer mechanism of an eEF2 kinase inhibitor. J. Biol. Chem. *286*, 43951–43958. https://doi.org/10.1074/jbc.M111.301291.

39. Chu, H.P., Liao, Y., Novak, J.S., Hu, Z., Merkin, J.J., Shymkiv, Y., Braeckman, B.P., Dorovkov, M.V., Nguyen, A., Clifford, P.M., et al. (2014). Germline quality control: eEF2K stands guard to eliminate defective oocytes. Dev. Cell *28*, 561–572. https://doi.org/10.1016/j.devcel.2014.01.027.

40. Wang, X., Li, W., Williams, M., Terada, N., Alessi, D.R., and Proud, C.G. (2001). Regulation of elongation factor 2 kinase by p90(RSK1) and p70 S6 kinase. EMBO J. *20*, 4370–4379. https://doi.org/10.1093/emboj/20.16.4370.

41. Browne, G.J., Finn, S.G., and Proud, C.G. (2004). Stimulation of the AMP-activated protein kinase leads to activation of eukaryotic elongation factor 2 kinase and to its phosphorylation at a novel site, serine 398. J. Biol. Chem. *279*, 12220–12231. https://doi.org/10.1074/jbc.M309773200.

42. Ebinu, J.O., Bottorff, D.A., Chan, E.Y., Stang, S.L., Dunn, R.J., and Stone, J.C. (1998). RasGRP, a Ras guanyl nucleotide- releasing protein with calcium- and diacylglycerol-binding motifs. Science *280*, 1082–1086. https://doi.org/10.1126/science.280.5366.1082.

43. Myers, D.R., Norlin, E., Vercoulen, Y., and Roose, J.P. (2019). Active tonic mTORC1 signals shape baseline translation in naive T cells. Cell Rep. *27*, 1858–1874.e6. https://doi.org/10.1016/j.celrep.2019.04.037.

44. Ksionda, O., Melton, A.A., Bache, J., Tenhagen, M., Bakker, J., Harvey, R., Winter, S.S., Rubio, I., and Roose, J.P. (2016). RasGRP1 overexpression in T-ALL increases basal nucleotide exchange on Ras rendering the Ras/PI3K/Akt pathway responsive to protumorigenic cytokines. Oncogene *35*, 3658–3668. https://doi.org/10.1038/onc.2015.431.

45. Depeille, P., Henricks, L.M., van de Ven, R.A.H., Lemmens, E., Wang, C.Y., Matli, M., Werb, Z., Haigis, K.M., Donner, D., Warren, R., and Roose, J.P. (2015). RasGRP1 opposes proliferative EGFR-SOS1-Ras signals and restricts intestinal epithelial cell growth. Nat. Cell Biol. *17*, 804–815. https://doi.org/10.1038/ncb3175.

46. Ho, L., Miller, E.L., Ronan, J.L., Ho, W.Q., Jothi, R., and Crabtree, G.R. (2011). esBAF facilitates pluripotency by conditioning the genome for LIF/STAT3 signalling and by regulating polycomb function. Nat. Cell Biol. *13*, 903–913. https://doi.org/10.1038/ncb2285.

47. Sims, R.J., 3rd, Nishioka, K., and Reinberg, D. (2003). Histone lysine methylation: a signature for chromatin function. Trends Genet. *19*, 629–639. https://doi.org/10.1016/j.tig.2003.09.007.

48. McCabe, M.T., Ott, H.M., Ganji, G., Korenchuk, S., Thompson, C., Van Aller, G.S., Liu, Y., Graves, A.P., Della Pietra, A., 3rd, Diaz, E., et al. (2012). EZH2 inhibition as a therapeutic strategy for lymphoma with EZH2-activating mutations. Nature *492*, 108–112. https://doi.org/10.1038/nature11606.

49. Hahn, W.C., and Weinberg, R.A. (2002). Rules for making human tumor cells. N. Engl. J. Med. *347*, 1593–1603. https://doi.org/10.1056/NEJMra021902.

50. Druckrey, H., Preussmann, R., Ivankovic, S., Schmidt, C.H., Mennel, H.D., and Stahl, K.W. (1964). Selective induction of bladder cancer in rats by Dibutyl- and N-butyl-N-Butanol(4)-Nitrosamine. Z. Krebsforsch. *66*, 280–290.

51. Fantini, D., Glaser, A.P., Rimar, K.J., Wang, Y., Schipma, M., Varghese, N., Rademaker, A., Behdad, A., Yellapa, A., Yu, Y., et al. (2018). A Carcinogen-induced mouse model recapitulates the molecular alterations of human muscle invasive bladder cancer. Oncogene *37*, 1911–1925. https://doi.org/10.1038/s41388-017-0099-6.

52. Toyoda, T., Akagi, J.I., Cho, Y.M., Mizuta, Y., Onami, S., Suzuki, I., and Ogawa, K. (2013). Detection of gamma-H2AX, a biomarker for DNA double-strand breaks, in urinary bladders of N -butyl- N -(4-Hydroxybutyl)-Nitrosamine-Treated rats. J. Toxicol. Pathol. *26*, 215–221. https://doi.org/10.1293/tox.26.215.

53. Jana, S., Deo, R., Hough, R.P., Liu, Y., Horn, J.L., Wright, J.L., Lam, H.M., Webster, K.R., Chiang, G.G., Sonenberg, N., and Hsieh, A.C. (2021). mRNA translation is a therapeutic vulnerability necessary for bladder epithelial transformation. JCI Insight *6*, e144920. https://doi.org/10.1172/jci.insight.144920.

54. Nguyen, T.M., Kabotyanski, E.B., Dou, Y., Reineke, L.C., Zhang, P., Zhang, X.H.F., Malovannaya, A., Jung, S.Y., Mo, Q., Roarty, K.P., et al. (2018). FGFR1-Activated translation of WNT pathway components with structured 5' UTRs is vulnerable to inhibition of EIF4A-dependent translation initiation. Cancer Res. *78*, 4229–4240. https://doi.org/10.1158/0008-5472.CAN-18-0631.

55. Truitt, M.L., Conn, C.S., Shi, Z., Pang, X., Tokuyasu, T., Coady, A.M., Seo, Y., Barna, M., and Ruggero, D. (2015). Differential requirements for eIF4E dose in normal development and cancer. Cell *162*, 59–71. https://doi.org/10.1016/j.cell.2015.05.049.

56. Bianco, C., Thompson, L., and Mohr, I. (2019). Repression of eEF2K transcription by NF-kappaB tunes translation elongation to inflammation and dsDNA-sensing. Proc. Natl. Acad. Sci. USA *116*, 22583–22590. https://doi.org/10.1073/pnas.1909143116.

57. Fresno, M., Jiménez, A., and Vázquez, D. (1977). Inhibition of translation in eukaryotic systems by harringtonine. Eur. J. Biochem. *72*, 323–330. https://doi.org/10.1111/j.1432-1033.1977.tb11256.x.

58. Kantarjian, H.M., Talpaz, M., Smith, T.L., Cortes, J., Giles, F.J., Rios, M.B., Mallard, S., Gajewski, J., Murgo, A., Cheson, B., and O'Brien, S. (2000). Homoharringtonine and low-dose cytarabine in the management of late chronic-phase chronic myelogenous leukemia. J. Clin. Oncol. *18*, 3513–3521.

59. Ingolia, N.T., Lareau, L.F., and Weissman, J.S. (2011). Ribosome profiling of mouse embryonic stem cells reveals the complexity and dynamics of mammalian proteomes. Cell *147*, 789–802. https://doi.org/10.1016/j.cell.2011.10.002.

60. Wolff, N.C., Pavía-Jiménez, A., Tcheuyap, V.T., Alexander, S., Vishwanath, M., Christie, A., Xie, X.J., Williams, N.S., Kapur, P., Posner, B., et al. (2015). High-throughput simultaneous screen and counterscreen identifies homoharringtonine as synthetic lethal with von Hippel-Lindau loss in renal cell carcinoma. Oncotarget *6*, 16951–16962. https://doi.org/10.18632/oncotarget.4773.

61. Gandhi, V., Plunkett, W., and Cortes, J.E. (2014). Omacetaxine: a protein translation inhibitor for treatment of chronic myelogenous leukemia. Clin. Cancer Res. *20*, 1735–1740. https://doi.org/10.1158/1078-0432.CCR-13-1283.

62. Mouw, K.W., and D'Andrea, A.D. (2014). Crosstalk between the nucleotide excision repair and Fanconi anemia/BRCA pathways. DNA Repair *19*, 130–134. https://doi.org/10.1016/j.dnarep.2014.03.019.

63. Chen, C.C., Feng, W., Lim, P.X., Kass, E.M., and Jasin, M. (2018). Homology-directed repair and the role of BRCA1, BRCA2, and related proteins in genome integrity and cancer. Annu. Rev. Cancer Biol. *2*, 313–336. https://doi.org/10.1146/annurev-cancerbio-030617-050502.

64. Marteijn, J.A., Lans, H., Vermeulen, W., and Hoeijmakers, J.H.J. (2014). Understanding nucleotide excision repair and its roles in cancer and ageing. Nat. Rev. Mol. Cell Biol. *15*, 465–481. https://doi.org/10.1038/nrm3822.

65. Walden, H., and Deans, A.J. (2014). The Fanconi anemia DNA repair pathway: structural and functional insights into a complex disorder. Annu. Rev. Biophys. *43*, 257–278. https://doi.org/10.1146/annurev-biophys-051013-022737.

66. Chen, Z., Trotman, L.C., Shaffer, D., Lin, H.K., Dotan, Z.A., Niki, M., Koutcher, J.A., Scher, H.I., Ludwig, T., Gerald, W., et al. (2005). Crucial role of p53-dependent cellular senescence in suppression of Pten-deficient tumorigenesis. Nature *436*, 725–730. https://doi.org/10.1038/nature03918.

67. Neiman, P.E., Thomas, S.J., and Loring, G. (1991). Induction of apoptosis during normal and neoplastic B-cell development in the bursa of Fabricius. Proc. Natl. Acad. Sci. USA *88*, 5857–5861. https://doi.org/10.1073/pnas.88.13.5857.

68. Wyllie, A.H., Rose, K.A., Morris, R.G., Steel, C.M., Foster, E., and Spandidos, D.A. (1987). Rodent fibroblast tumours expressing human myc and ras genes: growth, metastasis and endogenous oncogene expression. Br. J. Cancer *56*, 251–259. https://doi.org/10.1038/bjc.1987.186.

69. Hemann, M.T., Bric, A., Teruya-Feldstein, J., Herbst, A., Nilsson, J.A., Cordon-Cardo, C., Cleveland, J.L., Tansey, W.P., and Lowe, S.W. (2005). Evasion of the p53 tumour surveillance network by tumour-derived MYC mutants. Nature *436*, 807–811. https://doi.org/10.1038/nature03845.

70. Strasser, A., Harris, A.W., Bath, M.L., and Cory, S. (1990). Novel primitive lymphoid tumours induced in transgenic mice by cooperation between myc and bcl-2. Nature *348*, 331–333. https://doi.org/10.1038/348331a0.

71. Ying, Z., Sandoval, M., and Beronja, S. (2018). Oncogenic activation of PI3K induces progenitor cell differentiation to suppress epidermal growth. Nat. Cell Biol. *20*, 1256–1266. https://doi.org/10.1038/s41556-018-0218-9.

72. Wang, S.C., Nassour, I., Xiao, S., Zhang, S., Luo, X., Lee, J., Li, L., Sun, X., Nguyen, L.H., Chuang, J.C., et al. (2019). SWI/SNF component ARID1A restrains pancreatic neoplasia formation. Gut *68*, 1259–1270. https://doi.org/10.1136/gutjnl-2017-315490.

73. Liu, X., Li, Z., Wang, Z., Liu, F., Zhang, L., Ke, J., Xu, X., Zhang, Y., Yuan, Y., Wei, T., et al. (2022). Chromatin remodeling induced by ARID1A loss in lung cancer promotes glycolysis and confers JQ1 vulnerability. Cancer Res. *82*, 791–804. https://doi.org/10.1158/0008-5472.CAN-21-0763.

74. Lo, Y.H., Kolahi, K.S., Du, Y., Chang, C.Y., Krokhotin, A., Nair, A., Sobba, W.D., Karlsson, K., Jones, S.J., Longacre, T.A., et al. (2021). A CRISPR/Cas9-Engineered ARID1A-deficient human gastric cancer organoid model reveals essential and nonessential modes of oncogenic transformation. Cancer Discov. *11*, 1562–1581. https://doi.org/10.1158/2159-8290.CD-20-1109.

75. Robichaud, N., Sonenberg, N., Ruggero, D., and Schneider, R.J. (2019). Translational control in cancer. Cold Spring Harb. Perspect. Biol. *11*, a032896. https://doi.org/10.1101/cshperspect.a032896.

76. Howard, T.P., Oberlick, E.M., Rees, M.G., Arnoff, T.E., Pham, M.T., Brenan, L., DoCarmo, M., Hong, A.L., Kugener, G., Chou, H.C., et al. (2020). Rhabdoid tumors are sensitive to the protein-translation inhibitor homoharringtonine. Clin. Cancer Res. *26*, 4995–5006. https://doi.org/10.1158/1078-0432.CCR-19-2717.

77. Ulicna, L., Kimmey, S.C., Weber, C.M., Allard, G.M., Wang, A., Bui, N.Q., Bendall, S.C., Crabtree, G.R., Bean, G.R., and Van Rechem, C. (2022). The interaction of SWI/SNF with the ribosome regulates translation and confers sensitivity to translation pathway inhibitors in cancers with complex perturbations. Cancer Res. *82*, 2829–2837. https://doi.org/10.1158/0008-5472.CAN-21-1360.

78. Kaya-Okur, H.S., Wu, S.J., Codomo, C.A., Pledger, E.S., Bryson, T.D., Henikoff, J.G., Ahmad, K., and Henikoff, S. (2019). CUT&Tag for efficient epigenomic profiling of small samples and single cells. Nat. Commun. *10*, 1930. https://doi.org/10.1038/s41467-019-09982-5.

79. Henikoff, S., Henikoff, J.G., and Ahmad, K. (2021). Simplified epigenome profiling using antibody-tethered tagmentation. Bio. Protoc. *11*, e4043. https://doi.org/10.21769/BioProtoc.4043.

80. Buenrostro, J.D., Wu, B., Litzenburger, U.M., Ruff, D., Gonzales, M.L., Snyder, M.P., Chang, H.Y., and Greenleaf, W.J. (2015). Single-cell chromatin accessibility reveals principles of regulatory variation. Nature *523*, 486–490. https://doi.org/10.1038/nature14590.

81. Dobin, A., Davis, C.A., Schlesinger, F., Drenkow, J., Zaleski, C., Jha, S., Batut, P., Chaisson, M., and Gingeras, T.R. (2013). STAR: ultrafast universal RNA-seq aligner. Bioinformatics *29*, 15–21. https://doi.org/10.1093/bioinformatics/bts635.

82. Anders, S., Pyl, P.T., and Huber, W. (2015). HTSeq–a Python framework to work with high-throughput sequencing data. Bioinformatics *31*, 166–169. https://doi.org/10.1093/bioinformatics/btu638.

83. Robinson, M.D., McCarthy, D.J., and Smyth, G.K. (2010). edgeR: a Bioconductor package for differential expression analysis of digital gene

expression data. Bioinformatics *26*, 139–140. https://doi.org/10.1093/bioinformatics/btp616.

84. Xiao, Z., Zou, Q., Liu, Y., and Yang, X. (2016). Genome-wide assessment of differential translations with ribosome profiling data. Nat. Commun. *7*, 11194. https://doi.org/10.1038/ncomms11194.

85. Wickham, H. (2016). ggplot2: Elegant Graphics for Data Analysis (Springer-Verlag).

86. Law, C.W., Chen, Y., Shi, W., and Smyth, G.K. (2014). voom: precision weights unlock linear model analysis tools for RNA-seq read counts. Genome Biol. *15*, R29. https://doi.org/10.1186/gb-2014-15-2-r29.

87. Langmead, B., and Salzberg, S.L. (2012). Fast gapped-read alignment with Bowtie 2. Nat. Methods *9*, 357–359. https://doi.org/10.1038/nmeth.1923.

88. Ramírez, F., Ryan, D.P., Grüning, B., Bhardwaj, V., Kilpert, F., Richter, A.S., Heyne, S., Dündar, F., and Manke, T. (2016). deepTools2: a next generation web server for deep-sequencing data analysis. Nucleic Acids Res. *44*, W160–W165. https://doi.org/10.1093/nar/gkw257.

89. Eng, J.K., McCormack, A.L., and Yates, J.R. (1994). An approach to correlate tandem mass spectral data of peptides with amino acid sequences in a protein database. J. Am. Soc. Mass Spectrom. *5*, 976–989. https://doi.org/10.1016/1044-0305(94)80016-2.

STAR★METHODS

KEY RESOURCES TABLE

REAGENT or RESOURCE	SOURCE	IDENTIFIER
Antibodies		
PTEN (138G6), rabbit monoclonal	Cell Signaling Technology	Cat# 9559; RRID: AB_390810
Phospho-Akt (Ser473) (D9E), rabbit monoclonal	Cell Signaling Technology	Cat# 4060; RRID: AB_2315049
Akt1 (C-20), polyclonal	Santa Cruz Biotechnology	Cat# SC-1618; RRID: AB_630849
Alpha-Tubulin, mouse monoclonal	Sigma	Cat# T8203; RRID: AB_1841230
phospho-eIF2alpha (S51), rabbit monoclonal	Cell Signaling Technology	Cat# 3597; RRID: AB_390740
ATF-4 (D4B8), rabbit monoclonal	Cell Signaling Technology	Cat# 11815; RRID: AB_2616025
eIF4G (C45A4), rabbit monoclonal	Cell Signaling Technology	Cat# 2469; RRID: AB_2096028
eIF4E (A-10), mouse monoclonal	Santa Cruz Biotechnology	Cat# SC-271480; RRID: AB_10649368
eIF4A (C32B4), rabbit monoclonal	Cell Signaling Technology	Cat# 2013; RRID: AB_2097363
Phospho-4E-BP1 (Thr37/46) (236B4), rabbit monoclonal	Cell Signaling Technology	Cat# 2855; RRID: AB_560835
4E-BP1 (53H11), rabbit monoclonal	Cell Signaling Technology	Cat# 9644; RRID: AB_2097841
Phospho-eEF2 (Thr56),rabbit	Cell Signaling Technology	Cat# 2331; RRID: AB_10015204
eEF2, rabbit monoclonal	Cell Signaling Technology	Cat# 2332; RRID: AB_10693546
AURKB, rabbit polyclonal	Novusbio	Cat# NB-100-294; RRID: AB_2061617
FGFR3, rabbit anti-Human, mouse Fgfr3 Polyclonal	MyBioSource.com	Cat# MBS9212039
IGF2, mouse monoclonal	ThermoFisher	Cat# MA5-17096; RRID: AB_2538567
KIF22, rabbit polyclonal	Novusbio	Cat# NBP2-17053
ODC1, polyclonal	ThermoFisher	Cat# PA5-21362; RRID: AB_11154067
SKA1, rabbit polyclonal	Novusbio	Cat# NBP2-88277
BRCA2, rabbit polyclonal	Abcam	Cat# AB27976; RRID: AB_2067760
ERCC1, rabbit	Cell Signaling Technology	Cat# 3885; RRID: AB_2100142
ERCC2, rabbit	Cell Signaling Technology	Cat# 11963; RRID: AB_2797781
FANCC, rabbit polyclonal	Abcam	Cat# AB97575; RRID: AB_10679967
Phospho-AMPKα (Thr172) (40H9), rabbit monoclonal	Cell Signaling Technology	Cat# 2535; RRID: AB_331250
AMPK alpha, rabbit	Cell Signaling Technology	Cat# 2532; RRID: AB_330331
Tri-Methyl-Histone H3 (Lys27) (C36B11), rabbit	Cell Signaling Technology	Cat# 9733; RRID: AB_2616029
Histone H3, rabbit	Cell Signaling Technology	Cat# 9715; RRID: AB_331563
ARID1A/BAF250A (D2A8U), rabbit	Cell Signaling Technology	Cat# 12354; RRID: AB_2637010
Anti-Puromycin, clone 12D10, mouse monoclonal	EMD Millipore	Cat# MABE343; RRID: AB_2566826
IgG (H + L), rabbit HRP	Invitrogen	Cat# PI31460
IgG (H + L), mouse HRP	Invitrogen	Cat# PI31430
ARID1A, rabbit	Sigma	Cat# HPA005456; RRID: AB_1078205
ARID1A, mouse monoclonal	Santa Cruz	Cat# SC-32761; RRID: AB_673396
p-eEF2K (S366), rabbit polyclonal	Abcam	Cat# AB51227; RRID: AB_869561
p-eEF2K (S398), rabbit polyclonal	ECM Bio	Cat# EP5441

(*Continued on next page*)

Continued

REAGENT or RESOURCE	SOURCE	IDENTIFIER
eEF2K, rabbit monoclonal	Abcam	Cat# AB46787; RRID: AB_869559
p-p70RSK (T389), rabbit	Cell Signaling Technology	Cat# 9205; RRID: AB_330944
p70RSK, rabbit	Cell Signaling Technology	Cat# 9202; RRID: AB_331676
RASGRP1, rabbit polyclonal	Origene	Cat# TA358534
p44/42 MAPK (Erk1/2), rabbit	Cell Signaling Technology	Cat# 9102; RRID: AB_330744
MEK1/2, rabbit	Cell Signaling Technology	Cat# 9122; RRID: AB_823567
RSK1 p90 antibody [E4], rabbit monoclonal	Abcam	Cat# AB32114; RRID: AB_779068
Phospho-p44/42 MAPK (Erk1/2) (Thr202/Tyr204), rabbit	Cell Signaling Technology	Cat# 9101; RRID: AB_331646
Phospho-MEK1/2 (Ser217/221), rabbit	Cell Signaling Technology	Cat# 9121; RRID: AB_331648
phospho-p90RSK(Ser380) (D3H11), rabbit monoclonal	Cell Signaling Technology	Cat# 11989; RRID: AB_2687613
RASGRP1, polyclonal	ThermoFisher	Cat# PA5-25750; RRID: AB_2543250
p-Histone H2A.X (S139) (20E3), rabbit	Cell Signaling Technology	Cat# 9718; RRID: AB_2118009
EEF2/Elongation factor 2, rabbit polyclonal	Abcam	Cat# AB33523; RRID: AB_732081
p-eEF2 (T56), rabbit polyclonal	Abcam	ab53114; RRID: AB_869560
eEF2K, rabbit polyclonal	Aviva systems biology	Cat# OAAF00684
Phospho-eEF2K (Ser366), rabbit	Cell Signaling Technology	Cat# 3691; RRID: AB_2097313
Ki-67 (D3B5), rabbit monoclonal	Cell Signaling Technology	Cat# 12202; RRID: AB_2620142
Cleaved Caspase-3 (Asp175) (D3E9), rabbit monoclonal	Cell Signaling Technology	Cat# 9579; RRID: AB_10897512
ARID1A, rabbit	Sigma	Cat# HPA005456; RRID: AB_1078205
Alexa Fluor 594, mouse IgG (H + L)	Invitrogen	Cat# A-11032; RRID: AB_2534091
Alexa Fluor 488, rabbit IgG (H + L)	Invitrogen	Cat# A-11034; RRID: AB_2576217
Alexa Fluor 594, rabbit IgG (H + L)	Invitrogen	Cat# A-11037; RRID: AB_2534095
Alexa Fluor 647, rabbit IgG (H + L)	Invitrogen	Cat# A-21244; RRID: AB_2535812
HRP-labeled polymer, rabbit	Agilent	Cat# K4003; RRID: AB_2630375
CD326 (EpCAM) APC, rat	Invitrogen	Cat# 17-5791-80; RRID: AB_2734965
CD49f (Integrin alpha 6) PE, rat	ThermoFisher	Cat# 12-0495-82; RRID: AB_891474
anti-Cytokeratin 5, rabbit polyclonal	Biolegend Inc	Cat# PRB-160P; RRID: AB_291581
Tri-Methyl Histone H3 (Lys27) (C36B11), rabbit monoclonal	Cell Signaling Technology	Cat# 9733; RRID: AB_2616029
Guinea Pig anti-Rabbit IgG (Heavy & Light Chain)	Antibodies-online	Cat# ABIN101961; RRID: AB_10775589
Anti-acetyl-Histone H3 (Lys27) clone RM172, monoclonal	Millipore-Sigma	Cat# MABE647; RRID: AB_2893037
ARID1A, rabbit	Cell Signaling Technology	Cat# 12354; RRID: AB_2637010
Rabbit anti-IgG	Cell Signaling Technology	Cat# 2729; RRID: AB_1031062
Biological samples		
Patient-derived xenografts (PDX)1–3 [TM01029, TM00016, TM00024]	The Jackson Laboratory	http://www.jax.org

(*Continued on next page*)

Continued

REAGENT or RESOURCE	SOURCE	IDENTIFIER
Chemicals, peptides, and recombinant proteins		
N-Butyl-N-(4-hydroxybutyl)nitrosamine (BBN)	ThermoFisher	B0938
4-(N-Butyl-N-nitrosamino) butyric Acid (BCPN)	TCI	B3185
Homoharringtonine (HHT)	Carbosynth	FH15974
Puromycin Dihydrochloride	ThermoFisher	BP2956100
eEF2K inhibitor (A-484954)	Sigma	324516
GSK126	Selleckchem.com	S7061
DFMO	Tocris Bioscience	2761
Anti-FGFR3 Recombinant Antibody clone PRO-001	Creative bio labs	HPAB-0160-YC
Tamoxifen	Sigma	T5648
Hydrocortisone	Sigma	H4001
Collagenase type II	Life Technologies	17101015
Cell recovery solution	Corning	354253
B-27 Supplement	Gibco	17504–044
Murine EGF	Peprotech	315–09
A83-01	Tocris	2939
Y-27632 dihydrochloride	Sigma	Y0503
Doxycycline	ThermoFisher	AC446060050
Proteinase K	Sigma	3115879001
Mouse on Mouse (M.O.M.) Blocking Reagent	Vector Laboratories	MKB-2213
Pro-Long Gold Antifade mountant with DAPI	ThermoFisher	P36935
DAB solution	Agilent	K3467
Faramount mounting medium, Aqueous	Agilent	S302580
Histo Gel	Epredia	HG-4000-012
Cycloheximide	Sigma	C7698
Heparin sodium salt from porcine intestinal mucosa	Sigma	H3149
BioMag Plus Concanavalin A	Bangs laboratories, Inc.	BP531
Whatman® glass microfiber filters, Grade GF/C	Sigma	WHA1822024
LLC Liquid scintillation cocktail	ThermoFisher	50-904-0129
S35 EasyTagTM EXPRESS35S Protein Labeling Mix	Perkin Elmer	NEG772002MC
Critical commercial assays		
CellTiter-Glo® 2.0 Cell Viability Assay	Promega	G9242
Comet assay single cell gel electrophoresis assay kit	Trevigen	4250-050-K
Direct-zol Miniprep Plus kits	Zymo Research	ZR2070
TruSeq Stranded mRNA Library Prep Kit	Illumina	20020594
TruSeq RNA UD Indexes kit	Illumina	20022371
NovaSeq 6000 SP Reagent Kit	Illumina	20027464
Trans-Blot Turbo RTA Midi 0.2 μm PVDF Transfer Kit	Bio-Rad	1704273
Super Signal West Pico Chemiluminescent Substrate kit	ThermoFisher	PI34080
TMTpro18plex labeling reagent	ThermoFisher	A44521 and A52048
SimpleChIP Enzymatic Chromatin IP Kit	Cell Signaling Technology	9003S
Propidium Iodide Flow Cytometry Kit	Abcam	ab139418
GoTaq Green Master Mix	ThermoFisher	PRM7123
ERCC RNA Spike-In Mix	Invitrogen	4456740

(*Continued on next page*)

Continued

REAGENT or RESOURCE	SOURCE	IDENTIFIER
Deposited data		
CUT&Tag, RNA, and polysome-bound RNA sequencing	This paper	GSE201222
TMT mass spectrometry data	This paper	MSV000089875
Pipeline and analysis code	This paper	https://doi.org/10.5281/zenodo.7729526
Experimental models: Cell lines		
Human: HT1376	Gift from David MacPherson Lab (Fred Hutchinson Cancer Center).	N/A
Human: UMUC11	Gift from David MacPherson Lab (Fred Hutchinson Cancer Center).	N/A
Human: HT1197	Gift from David MacPherson Lab (Fred Hutchinson Cancer Center).	N/A
Human: KU1919	Gift from David MacPherson Lab (Fred Hutchinson Cancer Center).	N/A
Human: PrEC (Human Prostate Epithelial Cells)	Lonza	CC-2555
Experimental models: Organisms/strains		
Mouse: *Arid1a*$^{LoxP/LoxP}$	The Jackson Laboratory	Stock number: 027717
Mouse: *UBC-Cre*^{ERT2}	The Jackson Laboratory	Stock number: 008085
Mouse: *ROSA-LSL-Yfp*$^{KI/KI}$	The Jackson Laboratory	Stock number: 007903
Mouse: *K5-Cre*^{ERT2}	The Jackson Laboratory	Stock number: 029155
Mouse: *Eef2k*$^{-/-}$	A gift from Alexey G. Ryazanov (Rutgers University).	N/A
Mouse: *Rasgrp1*$^{-/-}$	A gift from Jeroen Roose lab (University of California, San Francisco).	N/A
Mouse: NOD-SCID γ IL-2	The Jackson Laboratory	Stock number: 005557
Oligonucleotides		
Primer for *Arid1a*$^{LoxP/LoxP}$ genotyping: Forward: 5′-GTAATGGGAAAGCGACTACTGGAG-3′ Reverse: 5′-TGTTCGTTTTTGTGGCGGGAG-3′	Integrated DNA Technologies	N/A
Primer for *UBC-Cre*^{ERT2} genotyping: Forward: 5′-GCGGTCTGGCAGTAAAAACTATC-3′ Reverse: 5′-GTGAAACAGCATTGCTGTCACTT-3′	Integrated DNA Technologies	N/A
Primer for *ROSA-LSL-Yfp*$^{KI/KI}$ genotyping: WT-Forward: 5′-CTGGCTTCTGAGGACCG-3′. Reverse: 5′-CAGGACAACGCCCACACA-3′ YFP- Forward: 5′-AGGGCGAGGAGCTGTTCA-3′. Reverse: 5′-TGAAGTCGATGCCCTTCAG-3′	Integrated DNA Technologies	N/A
Primer for *K5-Cre*^{ERT2} genotyping: WT-Forward: 5′-GCAAGACCCTGGTCCCAC-3′ Reverse: 5′-GGAGGAAGTCAGAACCAGGAC-3′ CreERT-Forward: 5′-GCAAGACCCTGGTCCTCAC-3′ Reverse: 5′-ACCGGCCTTATTCCAAGC-3′	Integrated DNA Technologies	N/A

(*Continued on next page*)

Continued

REAGENT or RESOURCE	SOURCE	IDENTIFIER
Primer for *Eef2k*$^{-/-}$ genotyping: WT-Forward: 5′GGCCGGCTGCTAGAGAGTGTC-3′. Reverse: 5′-CATCAGCTGATTGTAGTGGACATC-3′ eEF2K KO-Forward: 5′TGCGAGGCCAGAGGCC ACTTGTGTAGC-3′ Reverse: 5′-CAGGGCCTGCTTTCTTGGTGGCAG-3′	Integrated DNA Technologies	N/A
Primer for *Rasgrp1*qPCR: Forward: 5′-CTTCAACAC GCTGATGGCTGTG-3′. Reverse: 5′-GGACAGCAG TTCAGTCATCTCG-3′	Integrated DNA Technologies	N/A
GAPDH: Forward: 5′-CAATGAATACGGCTAC AGCAAC-3′. Reverse: 5′-AGGGAGATGCTCAGTGTTGG-3′	Integrated DNA Technologies	N/A
Primer for ChIP qPCR (*ARID1A* targeted region): Forward, 5′- CTTCGAATCCTGCCCCCATT-3′ Reverse, 5′- TCTTGGGCTGGGAGAGATGA-3′	Integrated DNA Technologies	N/A
ON-TARGETplus SMARTpool siRNA targeting *Arid1a:* GAAUAGGGCCUGAGGGAAA AGAUGUGGGUGGACCGUUA GCAACGACAUGAUUCCUAU GGACCUCUAUCGCCUCUAU	Dharmacon	Cat#L-017263-00-0005
Recombinant DNA		
pLenti-puro-ARID1A	Addgene	Cat#39478
pLenti6/TR	ThermoFisher	Cat#V48020
LV-Cre pLKO.1	a gift from Slobodan Beronja lab (Fred Hutchinson Cancer Research Center)	Addgene#25997
Rasgrp1-pEF6	A gift from the Jeroen Roose lab (University of California, San Francisco).	N/A
Software and algorithms		
voom	Law et al.[1]	https://rdrr.io/bioc/limma/man/voom.html
xtail	Xiao et al.[2]	https://anaconda.org/bioconda/xtail
R	The R Foundation	https://www.r-project.org
STAR2	Dobin et al.[3]	https://code.google.com/archive/p/rna-star/
HTSeq	Anders et al.[4]	https://htseq.readthedocs.io/en/master/
edgeR	Robinson et al.[5]	http://bioconductor.org
pheatmap		https://cran.r-project.org/web/packages/pheatmap/index.html
ggplot2	Wickham et al.[6]	https://ggplot2.tidyverse.org
Bowtie2 version 2.2.2	Langmead et al.[7]	https://bioweb.pasteur.fr/packages/pack@bowtie2@2.2.2
deepTools v3.5.1	Ramirez et al.[8]	https://deeptools.readthedocs.io/en/develop/
genomecov		https://bedtools.readthedocs.io/en/latest/content/tools/genomecov.html
computeMatrix	Ramirez et al.[8]	https://deeptools.readthedocs.io/en/develop/content/tools/computeMatrix.html
plotHeatmap	Ramirez et al.[8]	https://deeptools.readthedocs.io/en/develop/content/tools/plotHeatmap.html
Proteome Discoverer 2.5	ThemoFisher	https://thermo.flexnetoperations.com/control/thmo/login
SEQUEST	Eng et al.[9]	NA

(*Continued on next page*)

Continued

REAGENT or RESOURCE	SOURCE	IDENTIFIER
ImageJ	NIH	https://imagej.nih.gov/ij/download.html
Prism 9	GraphPad software	N/A
HALO	Indica labs	N/A
BioRender	BioRender	https://biorender.com/

RESOURCE AVAILABILITY

Lead contact

Further queries and reagent requests may be directed and will be fulfilled by the lead contact, Andrew C. Hsieh (ahsieh@fredhutch.org).

Materials availability

This study did not generate new unique reagents.

Data and code availability

- The CUT&Tag, RNA, and polysome sequencing data files are available at the GEO database. Accession number is listed in the key resources table. Mass spectrometry data and proteomics result files are available at the MassIVE database. Accession number is listed in the key resources table. All deposited data are publicly available as of the date of publication.
- The code used to process and analyze the data is available at Zenodo and is publicly available as of the date of publication. DOI is listed in the key resources table.
- All other data associated with this study are present in supplemental information and supplementary tables. Any additional information required to reanalyze the data reported in this paper is available from the lead contact upon request.

EXPERIMENTAL MODELS AND SUBJECT DETAILS

Mice

Arid1a$^{LoxP/LoxP}$ (https://www.jax.org/strain/027717, stock number: 027717), *ROSA-LSL-Yfp*$^{KI/KI}$ (https://www.jax.org/strain/007903, stock number: 007903), and *UBC-Cre*^{ERT2} (https://www.jax.org/strain/008085, stock number: 008085) mice were purchased from the Jackson Laboratory. eEF2K$^{-/-}$ animals were kindly provided by Alexey G. Ryazanov (Rutgers University). *UBC-Cre*^{ERT2};*ROSA-LSL-Yfp*$^{KI/KI}$;*Arid1a*$^{LoxP/LoxP}$ animals (mixed background) were bred to *Eef2k*$^{-/-}$ animals (C57BL/6) for one generation to produce progeny heterozygous at all loci (*ROSA-LSL-Yfp*$^{KI/+}$;*Arid1a*$^{LoxP/+}$;eEF2K$^{+/-}$) with or without *UBC-Cre*^{ERT2}. Heterozygous animals without *UBC-Cre*^{ERT2} were backcrossed once more to *ROSA-LSL-Yfp*$^{KI/KI}$;*Arid1a*$^{LoxP/LoxP}$ animals to reintroduce homozygosity at the *Arid1a* and *ROSA-LSL-Yfp*, while maintaining heterozygosity at the *Eef2k* locus (*ROSA-LSL-Yfp*$^{KI/KI}$;*Arid1a*$^{LoxP/LoxP}$;*Eef2K*$^{+/-}$; with and without *UBC-Cre*^{ERT2}). Of these progeny, animals with *UBC-Cre*^{ERT2}were bred to animals without *UBC-Cre*^{ERT2} to produce two parallel lineages, both in a consistent background with a single copy of *UBC-Cre*^{ERT2} (*UBC-Cre*^{ERT2};*ROSA-LSL-Yfp*$^{KI/KI}$;*Arid1a*$^{LoxP/LoxP}$;*Eef2k*$^{+/+}$ and *UBC-Cre*^{ERT2};*ROSA-LSL-Yfp*$^{KI/KI}$;*Arid1a*$^{LoxP/LoxP}$;*Eef2k*$^{-/-}$). The lineages were maintained separately with in-breeding.

K5-Cre^{ERT2} mice (https://www.jax.org/strain/029155, stock number: 029155) were purchased from the Jackson Laboratory. *ROSA-LSL-Yfp*$^{KI/KI}$;*Arid1a*$^{LoxP/LoxP}$ animals (mixed background) were bred to *K5-Cre*^{ERT2} animals (congenic C57BL/6 background) for one generation to produce progeny heterozygous at all loci (*K5-Cre*$^{ERT2/+}$;*ROSA-LSL-Yfp*$^{KI/+}$;*Arid1a*$^{LoxP/+}$). These animals were backcrossed once more to *ROSA-LSL-Yfp*$^{KI/KI}$;*Arid1a*$^{LoxP/LoxP}$ animals to reintroduce homozygosity at the *Arid1a* and *ROSA-LSL-Yfp* loci (*K5-Cre*$^{ERT2/+}$;*ROSA-LSL-Yfp*$^{KI/KI}$;*Arid1a*$^{LoxP/LoxP}$ and *K5-Cre*$^{+/+}$;*ROSA-LSL-Yfp*$^{KI/KI}$;*Arid1a*$^{LoxP/LoxP}$). The lineage was maintained with subsequent in-breeding of these two genotypes to maintain a single copy of CreERT.

NOD-SCID γ IL-2 mice (https://www.jax.org/strain/005557, stock number: 005557) were used for the preclinical trial. PDX models were obtained Jackson Laboratory (TM01029, TM00016, TM00024). We followed protocols approved by the Fred Hutchinson Cancer Center Animal Care and Use Committee (IACUC) for all mouse studies. The number of mice used for each study is included in figure legends. All studies were conducted using 50% male and 50% female mice. All comparison were made between littermates. For survival studies, the body weight of the mouse was recorded and monitored every two days for the duration of the survival trial. Mice were euthanized when they exhibit >20% weight loss or met euthanasia requirements by exhibiting pain and distress.

Cell culture

Cell lines used for this study include HT1376, KU1919, HT1197, UMUC11, and Human Prostate Epithelial Cells (Human PrEC). Mouse bone marrow stromal cells were derived from *WT* mice. HT1197 and HT1376 cells were cultured in Eagle's Minimum Essential Medium (ATCC, 30–2003) supplemented with 10% fetal bovine serum (Cytiva, SH3039603s), and 1% penicillin/streptomycin (Gibco, 15140-122). KU1919 cells were cultured in RPMI1640 (Gibco, 11875-119) supplemented with 10% fetal bovine serum, and 1%

penicillin/streptomycin. UMUC11 cells were cultured in DMEM (Gibco, 11965-092) supplemented with 10% fetal bovine serum, and 1% penicillin/streptomycin. These cell lines were maintained in a 37°C and 5% CO_2 incubator. All these cell lines were generously provided by MacPherson Lab (Fred Hutchinson Cancer Center). Human Prostate Epithelial Cells (Lonza, CC-2555) were cultured using Lonza's BulletKit media (Lonza, CC-3166) according to manufacturer's instructions. Mouse bone marrow stromal cells were generated by the following method. Briefly, bone marrow cells were isolated by flushing the tibia and femur bones of *WT* mice with PBS. Cells were filtered through a cell strainer and cultured in Iscove's modified Dulbecco's medium (Fisher, 12440053) supplemented with 15% fetal calf serum, 5% horse serum (Life Technology, 26050070), 10^{-5} M hydrocortisone (Sigma, H4001), 1% penicillin/streptomycin, and 10^{-4} M β-mercaptoethanol at 33°C.

Organoid culture

Organoid lines were generated either from normal murine bladder or bladder tumors. Minced tissues were treated with 5 mg/mL collagenase type II solution (Life Technologies, 17101015) diluted in Dulbecco's Modified Eagle's Medium for 1 h at 37°C, followed by a 5 min TrypLE (Gibco, 12604-039) treatment at 37°C. Digested tissues were further dissociated using a syringe with 18G needle, and single cells were obtained after passing through a cell strainer. Cells were plated using EHS (NIH and Corning) and cultured in organoid media for 5–7 days at 37°C. Organoid base media was prepared using Advanced DMEM/F12 (Gibco 12634010) supplemented with 20% B27 (Gibco, 17504-044), 10 mM HEPES, Glutamax (Fisher, 35050061), and 1.25 mM N-acetyl-L-cysteine (Sigma, A9165). Base media was also supplemented with 50 ng/mL EGF (Peprotech, 315-09), 100 ng/mL Noggin (conditioned media), 500 ng/mL R-spondin (conditioned media), 200 nM A83-01 (Tocris, 2939), and 10 μM Y-27632 (Sigma, Y0503). Organoids were passaged once every week.

METHOD DETAILS

ARID1A re-expression

Arid1a$^{fl/fl}$ organoid cells were plated at a density of 10,000 cells per 15 μL EHS in 24-well ultra-low attachment plates with lentivirus expressing (dox-inducible) pLenti-puro-ARID1A and pLenti6/TR. Organoids were cultured in organoid media (see organoid culture) for 96 h. Stable lines were generated using puromycin and blasticidin treatment.

Rasgrp1 re-expression

Arid1a$^{fl/fl}$ cells were transfected with Rasgrp1-pEF6 construct using Lipofectamine 3000. Stable lines were generated using blasticidin.

Urine BCPN analysis

Urine was collected from *WT*, *Arid1a*$^{fl/fl}$, and *Arid1a*$^{fl/fl}$*;Eef2k*$^{-/-}$ mice after 9 days of 0.075% BBN treatment. 5 μL of urine was analyzed on a Xevo QTof mass spectrometer. BCPN concentrations were calculated by comparing the urine BCPN measurements to standards of known BCPN (TCI, B3185) concentrations.

Immunoblot analysis

Cell lysates were prepared using RIPA buffer (Fisher, PI89900) containing phosphatase inhibitor (Sigma, 4906845001) and protease inhibitor cocktail (Sigma, 11836153001). The lysates were incubated on ice for 30 min with periodic vortexing, and centrifuged at 13,000 x g at 4°C for 10 min. The supernatants were subjected to SDS-PAGE and transferred to a PDVF membrane (Bio-Rad, 1704273). Membranes were blocked with 5% milk for 1 h at room temperature. Primary antibodies were diluted in 5% milk and incubated overnight at 4°C. Blots were incubated with HRP-conjugated secondary antibodies (goat anti–rabbit IgG [Fisher, PI31460] or goat anti–mouse IgG [Fisher, PI31430]) in 5% milk for 1 h at room temperature. West Pico (Fisher, PI34080) was used to detect immunoreactive bands on the blot using the ChemiDoc Touch Imaging System (Bio-Rad). The following primary antibodies were used: anti-Tubulin (Sigma, T8203), anti-ARID1A (Cell Signaling Technology, 12354), anti-PTEN (Cell Signaling Technology, 9559), anti-*p*-AKT(S473) (Cell Signaling Technology, 4060), anti-AKT1 (Santa Cruz Biotechnology, Sc-1618), anti-*p*-eIF2α (S51) (Cell Signaling Technology, 3597), anti-ATF4 (Cell Signaling Technology, 11815), anti-eIF4G (Cell Signaling Technology, 2469), anti-eIF4E (Santa Cruz Biotechnology, sc-271480), anti-eIF4A (Cell Signaling Technology, 2013), anti-*p*-4EBP1 (Cell Signaling Technology, 2855), anti-4EBP1 (Cell Signaling Technology, 9644), anti-*p*-eEF2 (T56) (Cell Signaling Technology, 2331), anti-eEF2 (Cell Signaling Technology, 2332), anti- AURKB (Novusbio, NB-100-294), anti-FGFR3 (Mybiosource, MBS9212039), anti-IGF2 (Fisher, MA5-17096), anti-KIF22 (Novusbio, NBP2-17053), anti-ODC1 (Fisher, PA5-21362), anti-SKA1 (Novusbio, NBP2-88277), anti-BRCA2 (Abcam, ab27976), anti-ERCC1 (Cell Signaling Technology, 3885), anti-ERCC2 (Cell Signaling Technology, 11963), anti-FANCC (Abcam, ab97575), anti-*p*-AMPK(Thr172) (Cell Signaling Technology, 2535), anti-AMPK (Cell Signaling Technology, 2532), anti-H3K27me3 (Cell Signaling Technology, 9733), anti-H3 (Cell Signaling Technology, 9715), anti-puromycin (EMD Millipore, MABE343), anti-Rasgrp1 (Origene, TA358534), anti-p70RSK (Cell Signaling Technology, 9202), anti-p-p70RSK (T389) (Cell Signaling Technology, 9205), anti-eEF2K (Abcam, ab46787), anti-*p*-eEF2K (S398) (ECM Bio, EP5441), anti-*p*-eEF2K (S366) (Abcam, ab51227), anti-ARID1A (Santa Cruz, SC-32761), and anti-ARID1A (Sigma, HPA005456).

Mouse genotyping

Mouse tissue was incubated in 1.67 mg/mL of Proteinase K solution (Sigma, 3115879001) overnight at 55°C, then subsequently extracted using phenol:chloroform:isoamyl alcohol (Ambion, AM9732) followed by ethanol precipitation. Genotypes were confirmed using PCR with GoTaq Green Master Mix (Promega PRM7123) followed by agarose gel electrophoresis (Bio-Rad, 161–3102). Primers used for genotyping PCR, *Arid1a* (forward, 5′-GTAATGGGAAAGCGACTACTGGAG-3′; reverse, 5′-TGTTCGTT TTTGTGGCGGGAG-3′), *UBC-Cre*^{ERT} (forward, 5′-GCGGTCTGGCAGTAAAAACTATC-3′; reverse, 5′-GTGAAACAGCATTGCTGT CACTT-3′; internal control: forward, 5′-CTAGGCCACAGAATTGAAAGATCT-3′; reverse, 5′-GTAGGTGGAAATTCTAGCATCATCC-3′), *ROSA-LSL-Yfp*$^{KI/KI}$ (WT: forward, 5′-CTGGCTTCTGAGGACCG-3′; reverse, 5′-CAGGACAACGCCCACACA-3′. YFP: forward, 5′-AGGGCGAGGAGCTGTTCA-3′; reverse, 5′-TGAAGTCGATGCCCTTCAG-3′), *K5-Cre*^{ERT2} (WT: forward, 5′-GCAAGACCCTGGT CCTCAC-3′; reverse, 5′-GGAGGAAGTCAGAACCAGGAC-3′. CreERT: forward, 5′-GCAAGACCCTGGTCCTCAC-3′; reverse, 5′-AC CGGCCTTATTCCAAGC-3′), *Eef2k*$^{-/-}$ (WT: forward, 5′-GGCCGGCTGCTAGAGAGTGTC-3′; reverse, 5′-CATCAGCTGATTGTAGTG GACATC-3′. eEF2K KO: forward, 5′TGCGAGGCCAGAGGCCACTTGTGTAGC-3′; reverse, 5′-CAGGGCCTGCTTTCTTGGTGG CAG-3′).

Hematoxylin and eosin staining (H&E), immunohistochemistry (IHC), immunofluorescence (IF)

Bladder samples were collected, fixed in 4% PFA, dehydrated with ethanol, and embedded in paraffin wax. Paraffin blocks were sectioned (5 μm) using a rotary microtome and H&E staining were performed at the Fred Hutchinson Cancer Center Histopathology Core. IHC staining was performed after rehydrating the tissue. In brief, antigen retrieval was performed by preheating in sodium citrate buffer (pH 6.0 or pH 9) solution for 7–30 min at 95°C–125°C in a pressure cooker. Hydrogen peroxidase (Vector Laboratories, SP-6000) treatment was done for 5 min to quench endogenous peroxides. Tissue was blocked in 1% BSA for 1 h. Primary antibodies were applied and incubated at room temperature for 1 h in a humidified chamber followed by secondary antibody (Envision system HRP-labeled polymer, Dako, K4003). Color development was achieved by applying DAB solution (Agilent Technology, K3467) for 2–5 min, depending on the primary antibody. The sections were counterstained with hematoxylin (Agilent technology, S3309), washed, and cover-slipped using aqueous-based mounting medium (Agilent Technology, S302580). All IHC slides were scanned using Aperio ScanScope AT Turbo (Leica Biosystems). Following primary antibodies were used for this study: anti-ARID1A (Sigma, HPA005456), anti-eEF2 (Abcam, ab33523), anti-*p*-eEF2 (T56) (Abcam, ab53114), anti-eEF2K (Aviva systems biology, OAAF00684), anti-ERK1/2 (Cell Signaling Technology, 9102), anti-*p*-ERK1/2 (Cell Signaling Technology, 9101), anti-MEK1/2 (Cell Signaling Technology, 9122), anti-*p*-MEK1/2 (Cell Signaling Technology, 9121), anti-p90RSK (Abcam, ab32114), anti-*p*-p90RSK (Cell Signaling Technology, 11989), anti-RASGRP1 (Fisher, PA5-25750), anti-Ki67 (Cell Signaling Technology, 12202), anti-γH2AX (Cell Signaling Technology, 9718), anti-CC3 (Cell Signaling Technology, 9579).

IF staining was performed in the following manner. Antigen retrieval was conducted by preheating in sodium citrate buffer (pH 6.0) for 30 min at 95°C in a pressure cooker. Tissue was blocked in 1% BSA solution for 2 h or in M.O.M blocking solution (Vector Laboratories, MKB 2213) for 1 h at room temperature, followed by blocking in 1% BSA solution for 2 h. Primary antibodies were applied overnight at 4°C in a humidified chamber, and secondary antibodies (Alexa Fluor 594: Invitrogen, A11032; Alexa Fluor 488: Invitrogen, A11034; Alexa Fluor 594: Invitrogen, A11037; Alexa 647: Invitrogen, A-21244) were applied for 1 h at room temperature. All IF slides were mounted using Pro-Long gold mounting media with DAPI (Fisher Scientific, P36935). IF slides were scanned using an Aperio Scanscope FL (Leica Biosystems). The following primary antibodies were used for IF study: anti-cytokeratin 5 (Biolegend Inc, PRB-160P), anti-puromycin (EMD Millipore, MABE343), anti-*p*-eEF2K(S366) (Cell Signaling Technology, 3691), anti-ARID1A (Sigma, HPA005456), anti-Cytokeratin 5 (Abcam, ab52635). Image analysis was done using semiautomated image analysis software (HALO, Indica Labs).

ChIP qPCR

5 x 10^6 cells were used per immunoprecipitation reaction using the SimpleChIP Enzymatic Chromatin IP Kit (Cell Signaling Technology, 9003S) as per manufacturers' instruction. Chromatin was cross-linked with 1% formaldehyde in PBS for 10 min at room temperature and quenched by the addition of 10x Glycine and incubation for 5 min at room temperature, followed by a wash with PBS. Crosslinked chromatin was fractionated by digestion with micrococcal nuclease (0.2 uL per IP) for 20 minutes at 37°C. This was followed by 6 cycles of sonication (20 seconds on, 30 seconds off, 50% amplitude) using a cup horn sonicator (Qsonica Q500). IPs were performed using 1:100 anti-ARID1A (D2A8U) (Cell Signaling Technology, 12354) and equivalent concentration of rabbit anti-IgG control (Cell Signaling Technology, 2729) at 4°C overnight. Crosslinks were reversed with Proteinase K at 65°C for 2 h and DNA was purified using the SimpleChIP Enyzmatic Chromatin IP Kit. ChIP-qPCR was performed as per manufacturers' instructions using Bio-Rad CFX384 Real-Time System using SsoAdvanced Universal SYBR Green Supermix (Bio-Rad, 172-5272). Primer sequences against ARID1A target regions used for ChIP-qPCR (forward, 5'- CTT CGA ATC CTG CCC CCA TT-3'; reverse, 5'- TCT TGG GCT GGG AGA GAT GA-3').

In vivo and *in vitro* puromycin incorporation assay

For the *in vivo* puromycin incorporation assay, mice were injected i.p. with 200 μL of 2.5 mM puromycin (Fisher, BP2956100) and euthanized after 1 hour. For *in vitro* puromycin incorporation assay, cells were treated with 1 μM puromycin for 30 minutes at 37°C.

RNA sequencing and polysome-bound RNA sequencing

Organoids were cultured for 96 hour before harvesting for RNA extraction or polysome profiling (see polysome profiling). The library preparation and sequencing were performed at the Fred Hutchinson Cancer Center Genomics Core. Polysome fractions were mixed 1:1 with TRIzol Reagent (Invitrogen, 15596-018) and stored at -80C until processing. The sub-polysome and polysome fractions were individually pooled and processed for sequencing. RNA was extracted from each pool using Direct-zol Miniprep Plus kits (Zymo, ZR2070) and concentrations were assessed by Qubit. ERCC RNA Spike-In Control Mix (Fisher, 4456740) was serial diluted (1:1000) and 2 μL was used for every 100ng of RNA. RNA-seq libraries were constructed using TruSeq Stranded mRNA Library Prep Kit (Illumina, 20020594) with the IDT for Illumina (TruSeq RNA UD Indexes: Illumina 20022371) following manufacturer's instructions. The sequencing was done on the Illumina NovaSeq 6000 using the SP-100 flow cell sequencing kit (Illumina, 20027464), 50PE run configuration.

In vitro [^{35}S]-methionine labeling assay

Cells were plated at a density of 10,000 cells per 50 μL EHS (NIH) and cultured with organoid media (see organoid culture). Cells were treated with 0.05 mCi/mL [^{35}S]-methionine (Perkin Elmer, NEG772002MC) at 37°C for 1 hour. Total cell lysates were prepared and subjected to immunoblot analysis. X-ray film was used to capture the radioactive signal. To check *de novo* protein synthesis in ARID1A re-expressing organoids, cells were treated with Doxycycline (0.1 μg/mL) for 48 h before [^{35}S]-methionine labeling.

Cell viability assay

WT bladder tumor organoids were established using following methods. Briefly, *WT* bladder tumor tissue chunks for *Arid1a* non-recombined *Arid1a*$^{fl/fl}$ mice were incubated in 5 mg/mL collagenase type II (Life Technologies, 17101015) diluted in Dulbecco's Modified Eagle's Medium for 1 hour at 37°C, followed by a 5 minute digestion with TrypLE (Gibco, 12604-039). Digested tissues were dissociated using a syringe with 18G needle, and single cells were obtained after passing through a cell strainer. Cells were plated at a density of 20,000 cells per 50 μL of EHS (NIH) on 24-well ultra-low attachment plates (Corning, 3473) and cultured in organoid media (see organoid culture) to establish *WT* bladder tumor organoids. *Arid1a*$^{fl/fl}$ bladder tumor organoids were generated from the *WT* parental line using lentivirus expressing Cre-recombinase (Addgene, 25997). To measure the differential cytotoxicity of homoharringtonine (HHT), the CellTiter-Glo 2.0 Assay (Promega, G9242) was used. Two thousand *WT* and *Arid1a*$^{fl/fl}$ tumor cells were embedded in 5 μL of Matrigel and plated on a 96-well plate in organoid media. One day post seeding, media was replaced with media containing either 100 nM or 1 μM of homoharringtonine (HHT). After a 48 hour HHT treatment, the CellTiter-Glo 2.0 Assay was performed according to manufacturer's instructions. HT1376, KU1919, HT1197, and UMUC11 cells (5000 cells/well) were plated on a 96-well plate. Cells were treated with various concentration of HHT (1, and 10 μM) at 48 hours after plating. After 24 hours of HHT treatment, the CellTiter-Glo 2.0 Assay was performed according to manufacturer's instructions.

siRNA knockdown

siARID1A (ON-TARGETplus SMARTpool siRNA: Dharmacon, J-017263-05) were transfected into human PrEC cells according to manufacturer's protocol. Briefly, human PrEC cells were plated in 6-well plate and siRNAs were transfected using lipofectamine 2000 transfection reagents (Fisher, 11668019). Cells were harvested 72 h after transfection and subjected to immunoblot to verify knockdown.

Polysome profiling

WT or Arid1a$^{fl/fl}$ cells were plated at a density of 10,000 cells per 50 μL EHS (NIH) and cultured with organoid media for 96 hours (see organoid culture). Cells were treated with 100 μg/mL (final concentration) cycloheximide (Sigma, C7698) for 10 minutes at 37°C. Cells were extracted from EHS by incubating in cell recovery solution (Corning, 354253) for 1 hour at 4°C. Cell pellets were lysed on ice in 350 μL of polysome lysis buffer (10 mM Tris-HCl pH 7.4 [Ambion, AM9851 (pH 7.0) and AM9856 (pH 8.0)], 132 mM NaCl (Ambion, AM9760G), 1.4 mM MgCl2 (Ambion, AM9530G), 19 mM DTT (Sigma, 43815), 142 μg/mL cycloheximide (Sigma, C7698), 0.1% Triton X-100 (Fisher, BP151), 0.2% NP-40 (Pierce, PI28324), 607 U/mL SUPERase-In RNase Inhibitor (Life Technologies, AM2696) with periodic vortex mixing. Lysates were clarified by centrifugation at 9300 x g for 5 minutes and supernatants were transferred to fresh tubes. Protein quantification was performed on each lysate by Bradford assay (Bio-Rad, 5000006) and analyzed using a BioTek Epoch Microplate Spectrophotometer. A portion of each lysate was saved as an input total RNA sample. For each lysate, 850 μg protein in 265 μL of the supernatant was layered onto 10% to 50% (w/v) linear sucrose gradients (Fisher, BP22010) containing 2 mM DTT (Sigma, 43815) and 100 μg/mL heparin (Sigma, H3149). The gradients were centrifuged at 37,000 rpm for 2.5 hours at 4°C in a Beckman SW41Ti rotor in Seton 7030 ultracentrifuge tubes. After centrifugation, samples were fractionated using a Biocomp Gradient Station (Biocomp) by upward displacement into collection tubes, through a Bio-Rad EM-1 UV monitor (Bio-Rad) for continuous measurement of the absorbance at 254 nm.

Ribosome half-transit time

Cells were plated at a density of 10,000 cells per 50 μL EHS in 24-well ultra-low attachment plates and cultured with organoid media (see organoid culture) for 96 hours. Cells were treated with 10 μCi/mL [^{35}S]-methionine (Perkin Elmer, NEG772002MC) and incubated at 37°C. At indicated time points (5, 10 and 15 minutes) after labeling, cells were harvested in ice-cold PBS containing 100 μg/mL cycloheximide. Cells were extracted from EHS using TrypLE treatment and resuspended in 250 μL of RBS buffer (10 mM NaCl,

10 mM Tris-HCl at pH 7.4, 15 mM MgCl2, 100 μg/mL heparin and protease inhibitor). 35 μL of lysis buffer (10% Triton X-100, 10% deoxycholate) was also added to lyse the cells. Cell suspension was incubated on ice for 10 minutes with periodic vortexing. Nuclei and mitochondria were separated by centrifugation for 5 minutes at 10,000 x g at 4°C. Supernatant (PMS) was removed and equal volume of polysome buffer (25 mM NaCl, 10 mM MgCl2, 25 mM Tris-HCl at pH 7.4, 0.05% Triton X-100, 0.14 M sucrose, 500 μg/mL heparin) was added. Polysomes were pelleted by centrifugation of half of the volume at 87,000 rpm for 2 hours using the TLA100 rotor and the supernatant (PRS) was removed. PMS represents nascent and completed proteins while PRS represents only completed proteins. Equal volume of PMS and PRS samples were precipitated on glass microfiber filters (Sigma, WHA1822024) using 20% TCA for 20 minutes on ice. Filters were washed with 10% TCA twice and once with ice-cold ethanol. Filters were air dried before taking counts. Liquid scintillation cocktail (Fisher, 50-904-0129) was added prior to liquid scintillation counting.

TMT mass spectrometry

Disulfide bond reduction/alkylation: Protein solutions (120 μg) were diluted to 2.4 μg/μL in 50 mM HEPES pH 8.5. Disulfide bonds within the proteins were reduced by adding tris (2-carboxyethyl) phosphine to a concentration of 5 mM and mixing at room temperature for 15 minutes. The reduced proteins were alkylated by adding 10 mM 2-chloroacetamide to a concentration of 10 mM and mixed in the dark at room temperature for 30 minutes. Excess 2-chloroacetamide was quenched by adding dithiothreitol to a concentration of 10 mM and mixing at room temperature for 15 minutes.

Protein precipitation and protease digestion: Samples (120 μg) were diluted to 1 μg/μL with 100 mM ammonium bicarbonate in a 1.5 mL Eppendorf low-bind tube. Protein precipitation was carried out as follows: 400 μL of methanol was added to the sample and vortexed for 5 seconds, 100 μL of chloroform was added to the sample and vortexed for 5 seconds, 300 μL of water was added to the sample and vortexed for 5 seconds, the samples were centrifuged for 1 minute at 14,000 x g, and the aqueous and organic phases were removed, leaving a protein wafer in the tube. The protein wafers were washed with 400 μL of methanol and centrifuged at 21,000 x g at room temperature for 2 minutes. The supernatants were removed and the pellets were allowed to air dry. The samples were resuspended in 70 μL 100 mM HEPES (pH 8.5) and digested with rLys-C protease (100:1, protein to protease ratio) with mixing at 37°C for 4 hours. Trypsin protease (100:1, protein to protease ratio) was added and the reaction was mixed overnight at 37°C.

TMTpro18plex labeling: Each TMTpro18plex labeling reagent (Fisher, A44521 and A52048) was brought up in 30 μL acetonitrile and added to their assigned digested peptide solution (100 μg), yielding a final organic concentration of 30% (v/v), and mixed at room temperature for 1 hour. A 2-μg aliquot from each sample was combined, dried to remove the acetonitrile, processed with a C18 Zip-tip, and analyzed via LC/MS as a "label check". The label check was used to check that the labeling efficiency of the TMT reagent exceeded 97% and to determine the volumes from each sample to be used for equalizing the protein amounts when combining the samples. After the label check, the reactions were quenched with hydroxylamine to a final concentration of 0.3% (v/v) and mixing for 15 minutes. The TMTpro18plex labeled samples were pooled at 1:1 ratio based on the equalization volumes determined in the label check and concentrated in a Speedvac to remove acetonitrile. Half of the material was desalted with an Oasis HLB 3cc cartridge and dried with a Speedvac.

bRP Fractionation: The desalted TMT sample was resuspended in 100 μL of 10 mM ammonium bicarbonate pH 8. The material was loaded on to a Zorbax 2.1 cm x 150 mm (5-μm particle size) Extend-C18 column connected to a HPLC equipped with a diode array detector and fraction collector. The sample was gradient-eluted from the column at a flowrate of 250 μL/min over 55 minutes using a combination of solvents "A" (10 mM ammonium bicarbonate) and "B" (acetonitrile). The elution profile used was as follows: from 0 to 5 minutes "B" was held at 1%, from 5 to 55 minutes "B" varied from 5% to 40% followed by an increase to 90% "B" over 5 minutes, and then a hold for an additional 5 minutes at 90% "B". The UV signal was monitored at 210 nm and fractions were collected every 50 seconds, resulting in 96 fractions. The fractions were combined into 24 pools by concatenating every 24th fraction into a pool (pool 1 = fractions 1, 25, 49, and 73, pool 2 = fractions 2, 26, 50, and 74, etc). The pools were taken to dryness by vacuum centrifugation and subsequently analyzed by LC/MS.

LC/MS: The dried basic reverse phase fractions were brought up in 2% acetonitrile in 0.1% formic acid (20 μL) and analyzed (2.5 μL) by LC/ESI MS/MS with a Easy1200 nLC coupled to a tribrid Orbitrap Eclipse with FAIMS pro mass spectrometer. In-line de-salting was accomplished using a reversed-phase trap column (100 μm × 20 mm) packed with Magic C_{18}AQ (5-μm, 200Å resin) followed by peptide separations on a reversed-phase column (75 μm × 270 mm) packed with ReproSil-Pur C_{18}AQ (3-μm, 120Å resin) directly mounted on the electrospray ion source. A 120-minute gradient from 4% to 44% B (80% acetonitrile in 0.1% formic acid/water) at a flow rate of 300 nL/min was used for chromatographic separations. The temperature of the chromatographic column was maintained at 40°C using a heating blanket. A spray voltage of 2300 V was applied to the electrospray tip in-line with a FAIMS pro source using varied compensation voltages of -40 V, -60 V, -80 V while the Orbitrap Eclipse instrument was operated in the data-dependent mode. MS survey scans were in the Orbitrap (Normalized AGC target value 300%, resolution 120,000, and max injection time 50 ms) using a 3 s cycle time and MS/MS spectra acquisition were also detected in the Orbitrap (Normalized AGC target value of 250%, resolution 50,000 and max injection time 100 ms) using higher energy collision-induced dissociation (HCD) activation with HCD collision energy of 38%.

Preclinical trials

Tumor pieces (1 × 1 × 1 mm) were implanted into the flank of 4-6 weeks old NOD-SCID γ IL-2 mice. Xenografts were measured every 2 days and tumor volume was calculated using the formula (L x W x W)/2, where L is the length of the tumor and W its width. When

tumors reached a total volume of 100 mm^3, animals were randomly selected for one of two treatment arms: Homoharringtonine (Carbosynth, FH15974) at 0.7 mg/kg dissolved in PBS or vehicle (PBS) twice daily by oral gavage.

CUT&Tag chromatin profiling

CUT&Tag was performed following the published protocol,[78] with some modifications. Briefly, cells were harvested and prepared into homogenous suspension in PBS, aliquoted with 10% DMSO and slow-frozen to −80°C in isopropanol freezing chambers. CUT&Tag was performed with native nuclei.[79] Cells were thawed at 37°C for 1 minute, washed twice with PBS and centrifugation at 600 x g for 3 minutes, and resuspended into ice-cold NE1 buffer (20mM K-HEPES pH 7.9, 10mM KCl, 10% Triton X-100, 20% Glycerol, 0.5 mM spermidine, and EDTA-free protease inhibitor). Cells were kept on ice for 10 minutes, centrifuged at 1400 x g for 3 minutes using a swinging-bucket rotor, pellets were resuspended in Wash buffer (20 mM Na-HEPES pH 7.5, 150 mM NaCl, 0.5 mM spermidine, and EDTA-free protease inhibitor), nuclei were counted using Vi-CELL Cell Viability Analyzer (Beckman Coulter) and aliquoted into 0.6 mL low-binding flip-cap tubes for CUT&Tag experiments.

500,000 nuclei were used for each CUT&Tag experiment targeting a histone posttranslational modification, while 200,000 nuclei were used for ARID1A. Bio-Mag Plus Concanavalin A coated magnetic beads (Bangs laboratories, BP531) were equilibrated with binding buffer (20 mM K-HEPES pH7.9, 10 mM KCl, and 1 mM each $CaCl_2$ and $MnCl_2$). To each sample, 10 μL of activated beads were added and held at room temperature for 5 minutes with occasional gentle mixing. Beads (with bound nuclei) were magnetized, supernatants were removed, beads were washed once with 400 μL antibody buffer (Wash buffer supplemented with 2 mM EDTA and 0.05% Digitonin), and resuspended in 200 μL antibody buffer containing the respective primary antibody in 1:100 v/v dilution (H3K27me3-Cell Signaling Technology, 9733 H3K27ac - Millipore-Sigma, MABE647; ARID1A – Cell Signaling Technology, 12354). Primary antibody incubations were performed on a rotating platform overnight at 4°C. Beads were magnetized, supernatant removed, washed once with 400 μL Dig-Wash (Wash buffer supplemented with 0.05% Digitonin), resuspended in 200 μL Dig-Wash containing guinea pig α-rabbit IgG secondary antibody (Antibodies-online.com, ABIN101961) at 1:100 dilution. Secondary antibody incubations were performed on a rotating platform for 30 minutes at room temperature. Beads were magnetized, supernatant removed, washed twice with 400 μL Dig-Wash to remove unbound antibodies, and resuspended in 200 μL Dig-Med buffer (Dig-Wash buffer, except containing 300 mM NaCl) with 1:200 dilution (~0.04 μM) of proteinA-Tn5 transposase fusion protein (pA-Tn5) pre-loaded with double-stranded adapters with 19-mer mosaic ends.[78] pA-Tn5 incubations were performed on a rotating platform for 1 hour at room temperature. Beads were magnetized, supernatant removed, washed three times with 400 μL Dig-Med to remove unbound pA-Tn5, and resuspended in 300 μL Tagmentation buffer (Dig-Med supplemented with 10 mM $MgCl_2$). Tagmentation reactions were performed by incubating samples at 37°C on a rotating platform for 1 hour. Tagmentation reactions were stopped by sequentially adding 10 μL of 0.5 mM EDTA, 3.1 μL of 10% SDS (1% final), and 2 μL of 20 mg/mL Proteinase K, mixed well, and incubated in 50°C water bath for 1 hour. DNA was extracted using phenol-chloroform-isoamyl alcohol (25:24:1), re-extracted with one volume $CHCl_3$, aqueous phase (~300 μL) was transferred to fresh tube, and DNA was precipitated by adding 900 μL ethanol overnight at -20°C followed by centrifugation for 45 minutes at 13,000 rpm and 4°C. Pellets were rinsed with 100% ice-cold ethanol, air-dried, dissolved in 30 μL 0.1 x TE (1 mM Tris pH 8, 0.1 mM EDTA) supplemented with RNase A (1:400 dilution of 10 mg/mL), and incubated in 37°C water bath for 15 minutes.

To amplify libraries, 21 μL DNA was mixed with 2 μL each of a universal i5 primer and a uniquely barcoded i7 primer,[80] using a different barcode for each sample, and 25 μL of NEB Next HiFi 2x PCR Master mix. Samples were placed in a thermocycler with heated lid using the following cycling conditions: 72°C for 5 minutes (gap filling); 98°C for 30 seconds (denaturation); 13 cycles of 98°C for 10 seconds and 63°C for 10 seconds (combined annealing and extension); final extension at 72°C for 1 minute, and held at 8°C. Post-PCR clean-up was performed using a double-sided clean-up method. 25 μL (0.5 X) of Ampure XP beads (Beckman Counter) was mixed with the libraries and incubated for 10 minutes at room temperature to remove large DNA fragments (>1300 bp). Beads were magnetized, supernatants were removed to fresh tubes and mixed with 45 μL (1.4 X - 0.5 X = 0.9 X) of Ampure XP beads and incubated for 10 minutes at room temperature. Beads were magnetized and the supernatants containing unused PCR primers were discarded. Beads were washed three times with 80% ethanol and eluted in 30 μL 10 mM Tris pH 8.0. Libraries were sequenced for 25 cycles in 25bp paired-end mode on the Illumina HiSeq 2500 platform or 50 bp paired-end mode on Illumina NextSeq 2000 at the Fred Hutchinson Cancer Center Genomics Shared Resource.

Flow cytometry

To isolate basal urothelial cells, bladder tissue was digested with collagenase II and generated single cell suspension (for details see organoid culture). Fluorescence-conjugated antibodies were then added to cell suspensions and stained for 30 minutes on ice. Live basal cells were separated by flow cytometry after staining with DAPI, EPCAM-APC (epithelial marker) and CD49f-PE (basal cell marker). 0.125 μg of EPCAM-APC (Invitrogen, 17-5791-80) and CD49f-PE (Fisher, 12-0495-82) were used respectively per sample containing $1x10^8$ cells.

Cell cycle analysis

Cells were fixed using pre-cooled 66% ethanol at 4°C for at 2 hours. Propidium iodide staining was performed following manufacturer's instruction (Abcam, ab139418). The cells were read using flow cytometry (Fortessa X50) and cell cycle phases were analyzed using FlowJo software.

Comet assay

The alkaline comet assay was performed using CometAssay kit (Trevigen, 4250-050-K) according to manufacturer's instructions. Briefly, organoids were treated with BCPN (100 μg/mL) for 96 hours. Cells were extracted from EHS using TrypLE and resuspended in PBS ($1x10^4$ cells/mL). The adjusted volume of cells was mixed with LMA (Low melting agarose) and plated onto comet slides. Comet slides were kept at 4°C for 30 minutes followed by overnight incubation in lysis buffer. The following day, comet slides were washed with water and immersed in alkaline unwinding solution (200mM NaOH, 1mM EDTA, pH>13) at 4°C for 1 hour in the dark. Slides were removed and placed into a horizontal electrophoresis tank containing alkaline electrophoresis buffer (200mM NaOH, 1mM EDTA, pH>13). Electrophoresis was performed at 21 V (300 mA) for 30 minutes. Slides were washed twice in water and kept in 70% ethanol for 5 minutes. SYBR Gold dye was used to stain the DNA and comet slides were scanned using Zeiss Axio Imager Z2 microscope (TissueGnostics, Austria). Damaged DNA molecules migrate slower than undamaged DNA leaving a characteristic appearance of a comet. Comet head represents undamaged DNA and length of the comet tails represent severity of damaged DNA.

Clonogenic assay

Cells were plated in 24-well plates at a density of 300 cells/well using 50% Matrigel for 24 hours, prior to the addition of 20 mM DFMO (Tocris Bioscience, 2761) and 10 μg/mL FGFR3 antibody (Creative bio labs, HPAB-0160-YC). DFMO containing media was removed and replaced every 48 hours. Colonies were counted after 10 days using the Evos FL cell imaging system.

Organoid embedding and staining

Organoids were fixed using 4% PFA for 2 hours at room temperature on a shaker followed by a 30 minute incubation on ice to achieve complete removal of EHS. Intact organoids were collected as a pellet after centrifugation at 1400 rpm for 5 min and washed with ddH_2O. The pellet was further washed with 0.2% BSA and organoids were mixed with HistoGel (Epredia, HG-4000-012). The organoid and HistoGel suspension was centrifuged at 1400 rpm for 5 minutes and kept on ice for 30 minutes. The solidified HistoGel structure was stored at 4°C until ready for processing and paraffin embedding. Organoid sections (5 μm) were deparaffinized in CitriSolv (Fisher, 4355121) for 10 minutes and rehydrated using 100% (2x), 90% (2x) and 70% (2x) ethanol for 5 minutes each. Antigen retrieval was performed by preheating in sodium citrate buffer (pH 6.0) solution for 10 minutes at 121°C in a pressure cooker. Organoid sections were blocked in 1% BSA solution for 1 hour followed by overnight incubation in primary antibody (anti-RASGRP1: Fisher, PA5-25750) at 4°C in a humidified chamber. Secondary antibody (Alexa-Fluor 594:Invitrogen, A11032) incubation was performed for 1 hour at room temperature. All slides were mounted using Pro-Long gold mounting media with DAPI (Fisher Scientific, P36935). Slides were scanned using an Aperio Scanscope FL (Leica Biosystems) and image analysis was done using semiautomated image analysis software (HALO, Indica Labs).

Drug administration

Tamoxifen: For all *in vivo* experiments, mice were given a total 30 mg of tamoxifen (Sigma,T5648) divided in 6 doses by oral gavage over the span of 3 weeks (2 doses/week). Tamoxifen was prepared in corn oil.

BBN: BBN (Fisher, B0938) was administrated (0.075%) in drinking water *ad libitum* for days as required for specific experiment (see experiment schema in figures).

eEF2K inhibitor (A-484954): For all eEF2K inhibitor experiments, mice received A-484954 (Sigma, 324516) daily (10 mg/kg body weight; IP) for 15 days.

QUANTIFICATION AND STATISTICAL ANALYSIS

RNA-sequencing and polysome sequencing analysis

Raw sequencing reads were checked for quality using FastQC (https://www.bioinformatics.babraham.ac.uk/projects/fastqc/). RNA-seq reads were aligned to the UCSC mm10 assembly using STAR2[81] and counted for gene associations against the UCSC genes database with HTSeq.[82] The normalized count data was used for subsequent Principal component analysis in R. Differential Expression analysis for RNA-Seq data was performed using R/Bioconductor package edgeR.[83] A $\log_2$fold change cutoff of 0.33 or 1.2 and FDR <0.05 was used to find transcriptionally regulated genes. Genome wide polysome to sub-polysome ratio analysis was performed using xtail.[84] Heatmaps were made using R/Bioconductor package pheatmap (https://CRAN.R-project.org/package=pheatmap). Volcano plots were made using ggplot2 in R.[85] For the ERCC Spike-In analysis, Bowtie2 was used for aligning the polysome sequencing data to 92 sequences from ERCC92 sequences. HTSeq-count was further used to the number of reads for each of the 92 sequences. The counts were normalized using voom.[86] Log_2 normalized counts were used to make scatterplots in R.

CUT&Tag data analysis

Paired-end *Mus musculus* reads were mapped to UCSC mm10 using Bowtie2 version 2.2.2[87] with parameters –end-to-end –very-sensitive –no-mixed –no-discordant -q –phred33 -I 10 -X 700. Continuous-valued data tracks (bedGraph and bigWig) were generated using genomecov in bedtools v2.30.0 (-bg option) and normalized as fraction of total counts. Genomic tracks were displayed using Integrated Genome Browser (IGB). Heatmaps and average plots were generated using computeMatrix and plotHeatmap operations in deepTools v3.5.1.[88] Scores were averaged over 50bp non-overlapping bins with the transcription start sites (TSS) of genes as

reference points and plotted as the mean. Box-and-whiskers plots were generated with GraphPad Prism. Average scores were computed for 2kb bins with TSS coordinates as the midpoint using the multi-Bigwig Summary operation in deepTools v3.5.1. Outliers (identified using the ROUT method, Q = 1%) were discarded. Boxes show the 75th and 25th percentiles and the median. The Tukey method was used to plot whiskers. CUT&Tag data were analyzed as described (https://www.protocols.io/view/cut-amp-tag-data-processing-and-analysis-tutorial-e6nvw93x7gmk/v1). Briefly, adapters were clipped and paired-end *M. musculus* reads were mapped to UCSC mm10 using Bowtie2 with parameters: –very-sensitive-local –soft-clipped-unmapped-tlen –dovetail –no-mixed –no-discordant -q –phred33 -I 10 -X 1000. Spike-in *E. coli* reads were mapped to Ensembl masked R64-1-1 with parameters: –end-to-end –very-sensitive –no-overlap –no-dovetail –no-unal –no-mixed –no-discordant -q –phred33 -I 10 -X 700.

TMT mass spectrometry data analysis

Protein database searching and quantification of TMT reporter ions was performed using Proteome Discoverer 2.5 (Thermo Scientific, San Jose, CA). The data were searched against a Mouse database (UP00000598 Human 030721) that included common contaminants (cRAPome). Searches were performed with settings for the proteolytic enzyme trypsin. Maximum missed cleavages were set to 2. The precursor ion tolerance was set to 10 ppm and the fragment ion tolerance was set to 0.6 Da. Dynamic peptide modifications were set for oxidation on methionine (+15.995 Da) and modifications on the protein N-terminus, consisting of acetylation (+42.011 Da), Met-loss (−131.040 Da), and Met-loss+Acetyl (−89.030 Da). Static modifications were set for TMTpro on any N-terminus (+304.207 Da), TMTpro on lysine (+304.207 Da), and carbamidomethyl on cysteine (+57.021 Da). Sequest HT was used for protein database searching and Percolator was used for peptide validation.[89]

Peptide to spectrum matches (PSMs) were filtered to a 1% false discovery rate and the resulting proteins were further filtered to a 1% false discovery rate. TMT channels were normalized to the largest channel intensity. Quantitative values were transformed to log2 values and missing data were imputed by 50% of global minimum intensity. To delineate differentially expressed proteins, both pairwise two-sample t-tests and Wilcoxon rank-sum tests were conducted (R package). The Benjamini-Hochberg procedure was used for controlling familywise error rate (FWER).

Ribosome half-transit time data analysis

[^{35}S]-methionine incorporation in nascent and completed protein within the PMS and completed protein within PRS was deduced by linear regression analysis. Ribosome half-transit time was calculated by the displacement of regression lines (PMS and PRS) at time 300 s.

%GC content in coding sequence analysis

To compare GC content of different classes of open reading frames (ORFs) (Figures S1L and S6A), *Mus musculus* UCSC genome sequence mm39 and Ensembl transcript annotations GRCm39 v106 were downloaded. Unique transcripts were identified for each protein coding gene by first checking for consensus coding sequence annotation (CCDSID) and then choosing the transcript with the highest support level. GC content of each CCDS ORF was calculated using letterFrequency function from the Biostrings R package. GC content for ORF groups that were transcriptionally up-regulated and those with high P/S ratio were plotted in comparison to the remaining ORFs using the geom_violin function from the ggplot2 R package. Statistical significance of differences in GC content between different ORF groups were calculated using the paired Wilcoxon test (wilcox.test R function).